Accepted Manuscript

Piperazine derivatives: Synthesis, inhibition of the *Mycobacterium tuberculosis* enoyl-acyl carrier protein reductase and SAR studies

Mariane Rotta , Kenia Pissinate , Anne Drumond Villela , Davi Fernando Back , Luis Fernando Saraiva Macedo Timmers , José Fernando Ruggiero Bachega , Osmar Norberto de Souza , Diógenes Santiago Santos , Luiz Augusto Basso , Pablo Machado

PII: S0223-5234(14)01066-6

DOI: 10.1016/j.ejmech.2014.11.034

Reference: EJMECH 7527

To appear in: *European Journal of Medicinal Chemistry*

Received Date: 11 July 2014

Revised Date: 13 November 2014

Accepted Date: 18 November 2014

Please cite this article as: M. Rotta, K. Pissinate, A.D. Villela, D.F. Back, L.F.S. Macedo Timmers, J.F.R. Bachega, O.N. de Souza, D.S. Santos, L.A. Basso, P. Machado, Piperazine derivatives: Synthesis, inhibition of the *Mycobacterium tuberculosis* enoyl-acyl carrier protein reductase and SAR studies, *European Journal of Medicinal Chemistry* (2014), doi: 10.1016/j.ejmech.2014.11.034.

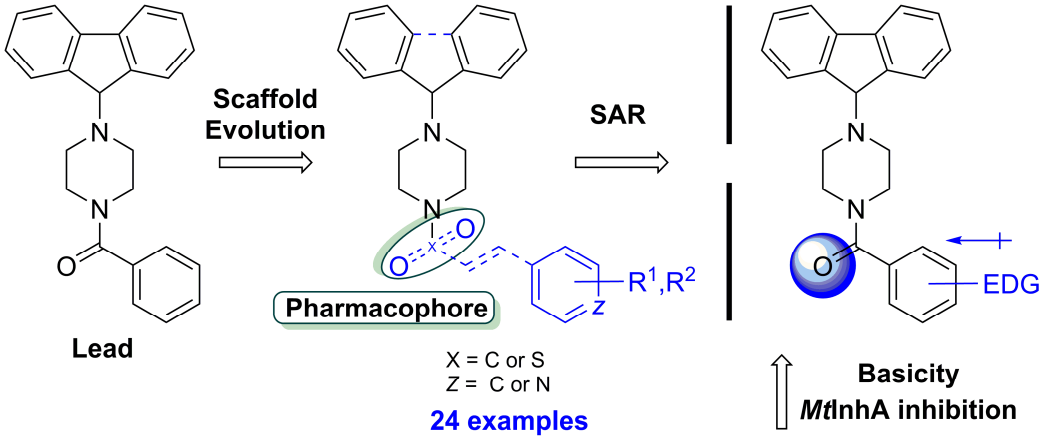

Piperazine derivatives: synthesis, inhibition of the *Mycobacterium tuberculosis* enoyl-acyl carrier protein reductase and SAR studies

Mariane Rotta [1,2], Kenia Pissinate [1,2], Anne Drumond Villela [1,3], Davi Fernando Back [4], Luis Fernando Saraiva Macedo Timmers [1,2,5], José Fernando Ruggiero Bachega [1,5], Osmar Norberto de Souza [1,2,5], Diógenes Santiago Santos [1,2*], Luiz Augusto Basso [1-3], Pablo Machado [1,2*]

[1]Instituto Nacional de Ciência e Tecnologia em Tuberculose, Centro de Pesquisas em Biologia Molecular e Funcional, Pontifícia Universidade Católica do Rio Grande do Sul, 90619-900, Porto Alegre, Rio Grande do Sul, Brazil

[2]Programa de Pós-graduação em Biologia Celular e Molecular, Pontifícia Universidade Católica do Rio Grande do Sul, 90619-900, Porto Alegre, Rio Grande do Sul, Brazil

[3]Programa de Pós-Graduação em Medicina e Ciências da Saúde, Pontifícia Universidade Católica do Rio Grande do Sul, 90619-900, Porto Alegre, Rio Grande do Sul, Brazil

[4]Departamento de Química, Laboratório de Materiais Inorgânicos, Universidade Federal de Santa Maria, 97105-900, Santa Maria, Rio Grande do Sul, Brazil

[5]Laboratorio de Bioinformática, Modelagem e Simulação de Biossistemas - LABIO, Pontifícia Universidade Católica do Rio Grande do Sul, 90619-900, Porto Alegre, Rio Grande do Sul, Brazil

*Corresponding authors. Phone/Fax: +55 51 3320 3629

E-mail addresses: diogenes@pucrs.br (D.S. Santos); pablo.machado@pucrs.br (P. Machado)

Abstract

The *Mycobacterium tuberculosis* NADH-dependent enoyl-acyl carrier protein reductase (*Mt*InhA) catalyzes hydride transfer to long-chain enoyl thioester substrates. *Mt*InhA is a member of the mycobacterial type II dissociated fatty acid biosynthesis system, and is the bona fide target for isoniazid, the most prescribed drug for tuberculosis treatment. Here, a series of piperazine derivatives was synthesized and screened as *Mt*InhA inhibitors, which resulted in the identification of compounds with IC_{50} values in the submicromolar range. A structure-activity relationship (SAR) evaluation indicated the importance of the chemical environment surrounding the carbonyl group for inhibition. In addition, the structure of one selected compound was supported by crystallographic studies, and experimental geometrical values were compared with semi-empirical quantum chemical calculations. Furthermore, the mode of inhibition and inhibitory dissociation constants were determined for the nine most active compounds. These findings suggest that these 9*H*-fluoren-9-yl-piperazine-containing compounds interact with *Mt*InhA at the enoyl thioester (2-*trans*-dodecenoyl-CoA) substrate binding site.

Keywords: *Mycobacterium tuberculosis*, tuberculosis, enoyl-ACP reductase, InhA inhibition, piperazines

Abbreviations: TB, tuberculosis; *M. tuberculosis*, *Mycobacterium tuberculosis*; MDR-TB, multidrug-resistant tuberculosis; HIV, human immunodeficiency virus; FAS, fatty acid synthase; ACP, acyl carrier protein; *Mt*InhA, enoyl-ACP reductase from *Mycobacterium tuberculosis*; NADH, nicotinamide adenine dinucleotide; INH, isonicotinic acid hydrazide; KatG, catalase-peroxidase; SAR, structure activity

relationship; HTS, high-throughput screening; K_{ii}, Inhibitory dissociation constant for the ESI complex; K_{is}, Inhibitory dissociation constant for the EI complex; MIC, minimal inhibitory concentration; TEA, triethylamine; HBTU, 2-(1*H*-benzotriazole-1-yl)-1,1,3,3-tetramethyluronium hexafluorophosphate; DMF, *N*,*N*-dimethylformamide; DD-CoA, 2-*trans*-dodecenoyl-CoA; DMSO, dimethyl sulfoxide; K_m, Michaelis constant; DMAP, 4-(*N*,*N*-dimethylamino)pyridine; PIPES, 1,4-piperazinediethanesulfonic acid

1. Introduction

Tuberculosis (TB) is an infectious disease primarily caused by *Mycobacterium tuberculosis* (*M. tuberculosis*), and it remains a major global health concern. According to the World Health Organization, an estimated 8.6 million new TB cases with approximately 1.3 million deaths were reported in 2012 [1]. The emergence of *M. tuberculosis* strains resistant to first- and second-line TB drugs has highlighted the need for novel and effective treatments [2]. Additional major concerns include TB-HIV coinfection and latent TB. In 2012, approximately 1.1 million of the estimated TB cases and 0.3 million deaths were described to occur among people who were HIV-positive [1]. In addition, one-third of the worldwide population has been reported to be at risk for reactivation from latent TB, which presents challenges in the eradication of this disease [3]. Within this context, worldwide efforts have been directed at the development of new anti-TB drugs [4]. Following more than 40 years, a new TB drug named bedaquiline was approved for clinical use [5]. However, the restrict indications of this drug, possible side effects [6], and the rapid appearance of new drug-resistant TB strains strengthen the need to continuing efforts towards the development of novel antimycobacterial compounds.

The mycobacterial type II dissociated fatty acid biosynthesis system (FAS-II) has emerged as an attractive, validated target for the development of novel anti-TB molecules [7]. The FAS-II system elongates acyl fatty acid precursors yielding the long carbon chain of the meromycolate branch of mycolic acids, the hallmark of mycobacteria [8,9]. Mycolic acids are high-molecular-weight α-alkyl, β-hydroxy fatty acids, which appear mostly as bound esters in tetramycolylpentaarabinosyl cluster in the mycobacterial cell wall [10,11]. These mycolic acids have been associated with *M. tuberculosis* virulence [9], the ability of *M. tuberculosis* to survive and replicate inside

macrophages and with the inability of many antimycobacterial compounds to penetrate into the *M. tuberculosis* cytosol [8,10]. The fatty acid precursors required for *M. tuberculosis* mycolic acid biosynthesis are synthesized by successive rounds of elongation and reduction reactions via the type I and type II fatty acid synthase (FAS-I and FAS-II) systems to yield, respectively, the α-branch and the meromycolate chain [10,11]. Encoded by the *inhA* gene, *M. tuberculosis* enoyl-ACP reductase (*Mt*InhA) catalyzes the final essential enzymatic step in fatty acid elongation in the FAS-II pathway, converting 2-*trans*-enoyl-ACP to acyl-ACP via a hydride transfer from the 4*S* hydrogen of NADH to the C3 position of the 2-*trans*-enoyl-CoA(ACP) substrate. *Mt*InhA has been identified as the primary target of isoniazid (INH), which is the frontline drug for TB chemotherapy, thereby validating this target for anti-TB drug discovery [12-14]. As a prodrug, INH requires oxidation by mycobacterial *katG*-encoded catalase-peroxidase (KatG) [15,16], which leads to the formation of the final covalent INH-NAD adduct that has been shown to be a slow, high-affinity competitive inhibitor of *Mt*InhA [13,17]. Notably, mutations in the *katG* gene have been linked to clinical resistance in 25-50% of newly diagnosed cases of INH-resistant TB [18,19]. Therefore, compounds able to directly inhibit *Mt*InhA, without KatG-assisted activation, could in theory target INH-resistant *M. tuberculosis* strains harboring *katG* gene mutations. We have thus been investigating compounds bound to transition metal complexes as self-activating species in the whole mycobacterial cell context with some encouraging results [20,21]. Moreover, virtual screening and pharmacophore-based approaches have resulted in the discovery of new *Mt*InhA inhibitors in the micromolar range [22]. In contrast to the recently reported methyl thiazoles that interact with *Mt*InhA in a "Tyr158-out" binding mode [23], direct inhibitors such as pyrrolidine carboxamides [24] and piperazine-indole derivatives [25] have explored polar

interactions involving a ribose hydroxyl, the Tyr158 hydroxyl and a hydrogen bond acceptor in the compounds. Consistent with our strategy [22], this substrate-protein-ligand interaction has been observed as a pharmacophoric point in virtual screening campaigns for novel *Mt*InhA inhibitors. However, the structural and electronic requirements for these hydrogen bond donor-acceptor pairs have not been extensively examined.

Therefore, in this study, we evaluated the inhibition of *Mt*InhA by piperazine-based compounds combined with structure activity relationship (SAR) studies. These compounds have been primarily obtained through high-throughput screening (HTS) approaches and exhibit submicromolar inhibition of *Mt*InhA enzyme activity (**Figure 1**) [25-27]. Herein, novel piperazine derivatives were synthesized, and the structure of one compound was elucidated using X-ray diffraction. In addition, the mode of inhibition, inhibitory dissociation constants (K_{ii} and/or K_{is}) were determined.

2. Results and discussion

2.1. Chemistry

First, we sought to synthesize 1-(9*H*-fluoren-9-yl)-piperazine derivatives bearing modifications around the carbonyl hydrogen bond acceptor. Using 1-(9*H*-fluoren-9-yl)-piperazine (**3**), compounds **2** and **4-8** were synthesized in low to good yields using classical methods (**Scheme 1**). The amides **2** and **4a-j** were obtained through acylation reactions of **3** using synthesized or commercially available benzoyl chlorides in the presence of triethylamine (TEA) as the base and dichloromethane (CH_2Cl_2) as the solvent. The reaction mixture was maintained at 0 °C during the addition of the reactants and then allowed to warm to 25 °C with subsequent stirring for 16 h. The 9*H*-

fluoren-9-yl-piperazines **2** and **4a-j** were isolated with 7-87% yield. Notably, one-pot synthesis of benzoyl chlorides following acylation reactions resulted in lower product yields in comparison with a direct acylation protocol. In addition, piperazine **4k** was synthesized from an active ester of pyridine-4-carboxylic acid and 1-(9*H*-fluoren-9-yl)-piperazine (**3**). The ester was formed in the presence of 2-(1*H*-benzotriazole-1-yl)-1,1,3,3-tetramethyluronium hexafluorophosphate (HBTU) and TEA using *N*,*N*-dimethylformamide (DMF) as solvent. The reaction mixture was stirred at 45 °C for 4 h to afford **4k** with 83% yield.

Direct sulfonylation was used for the synthesis of benzenesulfonyl derivatives **5a-b** to obtain the desired products in 61-82% yield. Additionally, to synthesize piperazine **6,** the cinnamic acid was previously prepared through condensation between benzaldehyde and malonic acid as previously described [28]. Thereafter, the α,β-unsaturated acid was converted to the respective chloride and reacted with 1-(9*H*-fluoren-9-yl)-piperazine (**3**) in a one-pot synthesis to afford **6** with 26% yield. The stereochemistry of the double bond was assigned based on the observed proton coupling constants (*J*) of 15 Hz. Finally, two S_N2 nucleophilic substitution reactions yielded compounds **7** and **8**. The 2-bromo-*N*-phenylacetamide precursor was synthesized as previously described [29] and was reacted with amine **3** in DMF in the presence of potassium carbonate at room temperature for 24 h. Piperazine **8** was synthesized via an identical protocol using (bromomethyl)benzene as the alkylating agent. Products **7** and **8** were obtained with 51% and 55% yield, respectively.

Compounds **10**-**12** were synthesized (**Scheme 2**) to evaluate the effect of increasing the degrees of freedom of phenyl-like groups inserted into the 1-(9*H*-fluoren-9-yl) ring on *Mt*InhA inhibition. This enhanced conformational flexibility may enable stronger hydrophobic interactions with the enzyme or result in entropy penalties in molecular

recognition [30]. Compound **10** was synthesized through acylation of 1-(diphenylmethyl)-piperazine (**9**) with benzoyl chlorides. The benzoyl chlorides were obtained from a commercial source or synthesized from the desired benzoic acids using of thionyl chloride. Independent of the source of the acylating agent, the reaction with amine **9** was performed in dichloromethane using TEA as the base at 0-25 °C for 16 h to obtain **10** with 15-87% yield. It is noteworthy that reactions were accomplished in one-pot procedures when benzoyl chlorides were generated from the respective acids. Furthermore, benzenesulfonyl chloride was reacted with amine **9** as previously described for piperazine **5** to afford compound **11** with 15% yield. Finally, piperazine **12** was obtained after chloride generation from cinnamic acid with concomitant acylation of 1-(diphenylmethyl)-piperazine. Compound **12** was isolated with 33% yield. Spectroscopic and mass spectrometry analyses of all of the synthesized compounds are consistent with the proposed chemical structures. As we sought to first evaluate any *Mt*InhA inhibitory activity by the synthesized compounds, the reaction conditions were not yet optimized.

2.1.1. Structure

The crystal structure of 9*H*-fluoren-9-yl-piperazine **4d** was determined by X-ray diffraction [31]. Carbocyclic 1-(9*H*-fluoren-9-yl) and 4-(4-fluorbenzoyl) moieties are attached to the piperazine ring (**Figure 2**). The crystal data and details of the data collection and structure refinement are summarized in **Table S1** (Supporting Information). Both the 9*H*-fluoren-9-yl and the 4-fluorbenzoyl moieties adopt a U-like conformation around the heterocyclic scaffold with the carbonyl group pointing out from the mean plane of the 4-fluorbenzyl substituent, as observed in the crystal

structure. The dihedral angle formed between C(24)-C(19)-C(18)-O is 44.5(2)°, whereas the angle observed for O-C(18)-N(2) is 121.3°, which results in near planarity of the amide group. As expected, the 9*H*-fluoren-9-yl ring exhibits a nearly planar structure inferred by the sum of the internal angles of the five-membered carbocycle [C(13)-C(12)-C(7)-C(6)-C(1)]. This sum was found to be 539.98° for compound **4d** and deviates only slightly from the ideal value of 540° for a regular pentagon.

To investigate the structural requirements of pharmacologically active compounds, utilization of computational methods that are able to reproduce the experimental data in good agreement is crucial. Thus, the geometrical parameters observed in piperazine **4d** were compared with semi-empirical AM1 [32] and PM3 [33-34] quantum chemical calculations. Incidentally, these methods have been used to analyze the conformational landscape of heterocyclic compounds, resulting in calculated values that are in good agreement with experimentally determined values [35]. The simple linear regressions of the experimental bond lengths and bond and dihedral angles from X-ray diffraction with semi-empirical calculated values exhibited good correlation coefficients. For bond lengths, both semi-empirical methods exhibited a similar correlation with the following experimental values: r = 0.947 for PM3 and r = 0.954 for AM1. These values account for, respectively, 89.8% and 91.0% of the variability in the bond lengths in the **4d** structure. The bond angles calculated from semi-empirical methods were also in good agreement with the experimentally determined bond angles, r = 0.935 and r = 0.945 for the PM3 and AM1 methods, respectively. The PM3 method accounts for 87.4% of the variability in the bond angles, whereas the AM1 approach accounts for 89.3% of this variation. However, the correlation between experimental and calculated values for the dihedral angles exhibited a significant difference between the two semi-empirical calculations. For the PM3 method, r = 0.891, which accounts for only 79.5% of the

variability in the dihedral angles in **4d**, whereas for the AM1 method, r = 0.988, which accounts for 97.7% of this variability. Thus, according to the magnitude of the correlation coefficients, the AM1 method is more suitable than the PM3 method to estimate the experimental geometrical parameters of the piperazines under study. In addition, this result represents another example in which the crystal structure is at or close to the global minimum energy conformation.

2.2. Inhibitory activity measurements

The reduction reaction of 2-*trans*-dodecenoyl-CoA (DD-CoA) catalyzed by *Mt*InhA was spectrophotometrically measured monitoring NADH oxidation to NAD^+ [36-37]. The enzyme inhibition assays were carried out in the presence of the synthesized compounds in a solution containing a final concentration of 1% dimethyl sulfoxide (DMSO) as the solvent. This concentration did not interfere with the assay conditions.

The synthesized lead-like **2** was assayed and exhibited an IC_{50} (the concentration of inhibitor that reduces the enzyme velocity by half) of 0.18 µM, which is 2-fold higher than the previously reported value of 0.09 µM [26] (**Table 1**). Modification of the hydrogen bond acceptor character from a carbonyl group to a sulfonyl moiety in piperazine **5a** resulted in a compound with an IC_{50} value of approximately 20 µM. This result may be attributed to a reduced hydrogen-bond basicity of sulfonamide compared to amide groups [38]. Notwithstanding, electron-donating groups tend to improve this basicity, compound **5b** containing a methyl group at the C2 position of the phenyl moiety exhibited reduced inhibition compared with the non-substituted counterpart (**5a**); IC_{50} > 50 µM. In an attempt to increase the hydrogen-bond basicity of the carbonyl

group and improve inhibitory activity, the α,β-unsaturated amide **6** was synthesized and evaluated. Unfortunately, the conjugated system was unable to inhibit *Mt*InhA activity and exhibited an IC_{50} > 50 µM. These findings suggest that steric factor was determinant on electronic feature of the proposed systems. Displacement of the position of the carbonyl through insertion of a methylene group resulted in drastically reduced inhibition by piperazine **7**. Notably, the amide was maintained while the insertion of the methylene group altered the conformational possibilities of the carbonyl moiety. This result suggests that the position of the carbonyl group does not tolerate even small spatial variations. Finally, the synthesis of compound **8** lacking an amide group afforded a piperazine that did not inhibit *Mt*InhA at 50 µM, emphasizing the importance of this hydrogen bond acceptor for *Mt*InhA inhibition.

An open system of the 9*H*-fluoren-9-yl ring was also evaluated to assess its influence (**10-12**) on *Mt*InhA enzyme inhibition. From the results summarized in **Table 1**, substitution of the planar system in **2** for the freely rotatable diphenylmethyl moiety in **10a** produced a compound that is nearly 88-fold less potent (IC_{50} = 16.0 µM) as compared to compound **2**. Indeed, the hydrophobic 9*H*-fluoren-9-yl moiety has been described as important for inhibition and mimics the fatty acid substrate within the substrate binding pocket [25]. This moiety is also present in the structure of recently described *Mt*InhA inhibitors [39-40]. Substitution at the C4 position of the aryl ring with a methyl group yields piperazine **10c**, which inhibited *Mt*InhA with an IC_{50} of 7.8 µM. By contrast, substitution at this position with a methoxy group (**10b**) greatly reduced inhibition by this compound (IC_{50} > 50 µM). Unexpectedly, even bioisosteric replacement of the 4-methyl (**10c**) with 4-Cl (**10d**) yielded a molecule with an IC_{50} > 50 µM, indicating fine tuning of this system. Indeed, except to **10a** and **10c**, none of the modifications on scaffold **10** generated molecules with IC_{50} values lower than 50 µM.

Similarly, sulfonyl (**11**) and cinnamic acid (**12**) derivatives did not inhibit *Mt*InhA catalysis at the maximum evaluated concentration of 50 µM.

In the next round of structural investigations, we evaluated substitutions at the C4 position in the phenyl ring of the lead-like compound **2**. The results summarized in **Table 1** for piperazines **4a-e** and **4k** indicated that, in general, electron-donating, hydrophobic and non-bulky groups exhibited enhanced *Mt*InhA inhibition. These findings are in accordance with previous reports, which have shown that enzyme inhibition is highly dependent on the chemical characteristics and size of groups around the phenyl substituent [26-27,41]. In addition, this solvent-exposed cavity is formed by polar and nonpolar groups and has been predicted to accommodate small and planar chemical groups [27,41].

It is noteworthy that from both ground-state and spectroscopic perspectives, halogens have been described to exhibit electron-donating characteristics from positive mesomeric effects (M+) [42]. Accordingly, nitro-substituted compound **4e** exhibited an IC_{50} > 50 µM. This result can be attributed to the ability of electron withdrawing groups to reduce the ability of the carbonyl to act as a hydrogen bond acceptor. Between the evaluated moieties, the nitro moiety was the most electron withdrawing group evaluated at the C4 position of the phenyl ring presenting negative mesomeric and inductive effects (M- and I-). Such features may account for the reduced inhibition by compound **4e**. It is important to mention that nitro is a planar group in the same way as the indole substituent present in piperazine derivative **1**, which was able to produce an inhibitor of *Mt*InhA with an IC_{50} of 0.16 µM [25]. Therefore, for **4e** activity, the electronic effect, instead of steric effects, seems to be crucial.

Piperazine **4k** was proposed with the objective of evaluating the effect of a compound with a molecular volume similar to lead-like **2** but showing distinct electronic and hydrophobic characteristics. Pyridine derivative **4k** showed moderate inhibition on *Mt*InhA activity with an IC_{50} of 9.7 µM, which was nearly 53-fold less potent than benzyl-substituted compound **2**.

Regarding electron-donating groups, the methoxy-substituted piperazine **4a** exhibited an IC_{50} of 2.9 µM, whereas the 4-methyl group in **4b** was able to inhibit *Mt*InhA with an IC_{50} of 0.22 µM (0.40 µM [26]), which is submicromolar and comparable to lead-like compound **2**. Once more, classical bioisosteric replacement of a methyl group with a chloro substituent yielded compound **4c**, which was approximately 10-fold less effective for *Mt*InhA inhibition than the methyl derivative **4b**. By contrast, fluoro-substituted **4d** maintained inhibition in the submicromolar range, with an IC_{50} of 0.40 µM. This result shows that piperazine **4b** (4-methyl) is nearly 2-fold more potent than **4d** (4-fluoro), based on the magnitude of the IC_{50} values. Although 4-fluoro and 4-methyl share identical mesomeric effects, their inductive effects are opposite: fluoro substitution reduces the electron density along the sigma bonds, whereas the methyl group increases this electron density. Thus, 4-methyl (**4b**) can increase the basicity of the carbonyl group and maintain a more hydrophobic environment around the benzyl ring, leading to enhanced inhibition of *Mt*InhA compared to the 4-fluoro-substituted compound (**4d**).

In evaluating the position of the methyl in the benzyl ring, the inhibition data indicated a preference for the C4 and C3 positions in comparison with 2-substituted derivatives. It is noteworthy that hydrogens at the C2 and C3 positions of the phenyl ring have been described as having weak hydrogen bonds with NADH [41]. Piperazine **4f** (3-methyl) exhibited an IC_{50} of 0.25 µM, whereas compound **4g** (2-methyl) inhibited

*Mt*InhA with an IC_{50} of 6.0 µM. Considering the fluorinated molecules **4d** and **4h-i**, the C3 position was slightly preferred for enhanced inhibitory potency in comparison with the C4 and C2 positions, as **4h** (3-fluoro) and **4i** (2-fluoro) exhibited IC_{50} values of 0.24 µM and 0.36 µM, respectively. Finally, 2,5-difluoro-substituted **4j** exhibited reduced inhibitory potency on the catalytic activity of *Mt*InhA, with an IC_{50} of 1.6 µM. According to the structures of **4g** and **4i** studied by docking simulations, the presence of the methyl group at the C2 position of the aryl moiety causes steric hindrance due to the restricted space in the cavity formed by Met103, Tyr158, and Met161 residues of *Mt*InhA (**Figure 3**). It is noteworthy that halogen substituents typically form multiple interactions, as well as participate in desolvation effects in ligand-protein complexes [43]. Based on the observed distances and the sum of the van der Walls radii, the fluoro group does not appear to form hydrogen bonds with *Mt*InhA or NADH. Therefore, steric hindrance, halogen-mediated interactions, and desolvation effects may account for the better activity of compound **4i** compared to **4g**.

2.2.1. Determination of K_i values for select *Mt*InhA inhibitors

Using a threshold of 3 µM for the IC_{50} values, nine compounds (**2**, **4a-d**, **4f** and **4h-j**) were selected for additional studies on the mode of inhibition (uncompetitive, noncompetitive or competitive) of *Mt*InhA. It is noteworthy that none of these molecules exhibited time-dependent inhibitory activity up to 30 min of preincubation with *Mt*InhA (data not shown), suggesting rapid equilibrium processes. Accordingly, the mode of inhibition could be determined from Lineweaver-Burk plots and data fitting to appropriate equations to give values for the inhibition constants (K_{ii} and/or K_{is}) [44] (**Table 2**). When the substrate DD-CoA was fixed at a non-saturating concentration and

NADH was varied in the presence of fixed-varying concentrations of the compounds, the double reciprocal plots yielded parallel lines (Supporting Information). These results indicated that all of the evaluated compounds are uncompetitive inhibitors with respect to NADH. Fitting the data to Eq. 2 yielded the values for the ternary complex inhibition constants (K_{ii}), with values ranging from 0.147–1.95 μM. (**Table 2**). The inhibitory profile suggests that these inhibitors exhibit low affinity to the free enzyme and a nearly complete binding preference for the enzyme-substrate (ES) complex to yield an inactive enzyme-substrate-inhibitor (ESI) complex [44,45]. Moreover, the binding of these compounds to the *Mt*InhA:NADH binary complex corroborate the proposed hydrogen bonding network between the pharmacophore-like carbonyl group, hydroxyl group of the nicotinamide ribose and Y158 in the formation of the ESI complex [25-26,42].

Furthermore, when NADH was fixed at a non-saturating concentration and the DD-CoA substrate was varied in the presence of fixed-varying concentrations of the piperazines **2**, **4a**, **4c**, **4f**, and **4i-j**, a noncompetitive inhibition profile was obtained, as indicated by the lines that intercept on left of *y*-axis in the double reciprocal plots. Fitting the data to Eq. 3 yielded K_{is} values ranging from 0.100–2.77 μM and K_{ii} values ranging from 0.348–7.22 μM (**Table 2**). Except for compound **4c**, inhibitors exhibited $K_{is} < K_{ii}$, indicating a binding preference for the free enzyme in comparison to binding to the *Mt*InhA-DD-CoA binary complex. These results suggested that the compounds could interact with the DD-CoA binding site even with a noncompetitive signature [44]. Aiming to shed light on this issue, saturating concentrations of DD-CoA and NADH were used to assay lead-like compound **2**. In these assays, when the DD-CoA concentration was maintained at approximately 135 μM ($K_m \cong 45$ μM [36]) and the NADH concentration was varied from 10–120 μM, the uncompetitive inhibition with respect to NADH was maintained (Supporting Information). However, when the NADH

concentration was saturating at 240 µM (K_m ≅ 60 µM [36]) and the DD-CoA concentration was varied from 15-200 µM, a competitive inhibition profile with respect to the DD-CoA substrate was observed for piperazine **2** (Supporting Information). Taken together kinetics results and crystallographic studies of the analogous compound **1** strengthened the hypothesis that compound **2** interacts with the enzyme at the fatty acid binding site [25].

Inhibition assays for **4b**, **4d** and **4h** indicated that these compounds are competitive inhibitors with respect to the DD-CoA substrate, as the lines intersected at a single value on the *y*-axis of the double-reciprocal plots (Supporting Information). Fitting the data to Eq. 4 yielded K_{is} values ranging from 0.101–0.338 µM (**Table 2**). As proposed for **2**, these compounds likely interact with the fatty acid binding site of *Mt*InhA.

Finally, MIC determination for the most potent *Mt*InhA inhibitors was accomplished *in vitro* using the *M. tuberculosis* H37Rv strain (Supporting Information). Although the poor solubility of the evaluated compounds precluded a more accurate MIC determination, piperazines **4b** and **4d** exhibited moderate antimycobacterial activity, with a MIC of 25 µg/mL (≈ 67.8 µM).

3. Conclusion

The inhibition of *Mt*InhA activity by piperazine derivatives was assessed using kinetic assays. Additionally, insights into the structural requirements for effective enzyme inhibition and the determination of the mode of inhibition of the synthesized compounds emphasized the pharmacophore role of the amide carbonyl group in the formation of the ESI complex. The results presented herein suggest that modulation of the hydrogen bond acceptor may be a critical step in the optimization of *Mt*InhA

inhibitors. Future challenges will include the design of novel piperazine derivative compounds for the fatty acid binding site maintaining the drug-like properties that allow for cellular potency. Finally, our results may provide important details for the design of novel structures to interact with a clinically validated TB target, thereby prompting the discovery of novel antituberculosis agents.

4. Experimental Section

4.1. Synthesis and structure: apparatus and analysis

All common reactants and solvents were used as obtained from commercial suppliers without further purification. Melting points were determined using a Microquímica MQAPF-302 apparatus. ^{1}H NMR spectra were acquired on an Anasazi EFT-60 spectrometer (^{1}H at 60.13 MHz) at 30 °C. ^{13}C NMR spectra were acquired on a Varian (Federal University of Rio Grande do Sul, UFRGS/Brazil) spectrometer (^{13}C at 100.6 MHz) at 25 °C. $CDCl_3$ was used as the solvent, and TMS was used as an internal standard in 5-mm samples tubes. Chemical shifts are expressed in ppm, and *J* values are given in Hz. High-resolution mass spectra (HRMS) were obtained for all compounds on an LTQ Orbitrap Discovery mass spectrometer (Thermo Fisher Scientific, Bremen, Germany). This hybrid system combines the LTQ XL linear ion trap mass spectrometer with an Orbitrap mass analyzer. The experiments were performed using direct infusion of the sample in a solution of acetonitrile (50%), methanol (50%), and formic acid (0.1%), with a flow of 5 μL min^{-1} in positive-ion mode using electrospray ionization. Elemental composition calculations were performed using a specific tool included in the Qual Browser module of the Xcalibur (Thermo Fisher Scientific, release 2.0.7) software. Fourier transform infrared (FTIR) spectra were recorded using a universal

attenuated total reflectance (UATR) attachment on a PerkinElmer Spectrum 100 spectrometer in the wavenumber range of 650-4000 cm^{-1} with a resolution of 4 cm^{-1}. Crystal data were collected using a Bruker APEX II CCD area-detector diffractometer and employing graphite-monochromatized MoKα radiation. The structures from the ligand and the complex were determined by direct methods using *SHELXS-97* [46]. Subsequent Fourier-difference map analyses yielded the positions of the non-hydrogen atoms. Refinements were performed using the *SHELXL-97* package [47]. All refinements were performed using full-matrix least-squares on F^2, with anisotropic displacement parameters for all non-hydrogen atoms. Hydrogen atoms were included in the refinement in calculated positions. Finally, the structure was rendered using ORTEP-3 for Windows [48].

*4.2. General procedure for the synthesis of piperazines **2**, **4a-j** and **10a-f***

Method i: Benzoic acid (1 mmol) was reacted with a solution of thionyl chloride in CH_2Cl_2 (1 M, 6 mL) in refluxing toluene (3 mL) for 5 h. After cooling to room temperature, the solvent was evaporated under reduced pressure. The obtained benzoyl chloride was dissolved in dry CH_2Cl_2 (5 mL), and the resultant solution was cooled to 0 °C. To this solution, TEA (4.4 mmol, 0.444 g), 1-(9*H*-fluoren-9-yl)-piperazine (**3**) (1.1 mmol, 0.275 g) or 1-(diphenylmethyl)-piperazine (**9**) (1.1 mmol, 0.277 g) in dry CH_2Cl_2 (5 mL) was added dropwise. After the addition, the reaction mixture was stirred for 16 h at room temperature. Subsequently, the solution was washed with aqueous HCl (10%, v/v, 3 x 15 mL), a saturated $NaHCO_3$ solution (1 x 15 mL), and aqueous NaCl (5%, w/v, 1 x 15 mL). Finally, the organic layer was dried over anhydrous magnesium sulfate. The mixture was filtered, and the solvent was evaporated under reduce pressure. When necessary, the products were purified using silica gel chromatography with

CH_2Cl_2/methanol (20:5, v/v) as the mobile phase. This protocol was used for the synthesis of 9*H*-fluoren-9-yl-piperazines **2**, **4a**, **4c-e**, **4h-i** and 1-(diphenylmethyl)-piperazines **10a-b** and **10d-e**. The crystal used for the data collection was obtained by recrystallization of compound **4d** from hexane followed by slow evaporation at room temperature.

Method ii: Benzoyl chloride (1.0 mmol) was solubilized in dry CH_2Cl_2 (5 mL), and the resultant solution was cooled to 0 °C. To this solution, TEA (4.4 mmol, 0.444 g), 1-(9*H*-fluoren-9-yl)-piperazine (**3**) (1.1 mmol, 0.275 g) or 1-(diphenylmethyl)-piperazine (**9**) (1.1 mmol, 0.277 g) in dry CH_2Cl_2 (5 mL) was added dropwise. After the addition, the reaction mixture was stirred for 16 h at 25 °C. Subsequently, the solution was washed with aqueous HCl (10%, v/v, 3 x 15 mL), a saturated $NaHCO_3$ solution (1 x 15 mL), and aqueous NaCl (5%, w/v, 1 x 15 mL). Finally, the organic layer was dried over anhydrous magnesium sulfate. The mixture was filtered, and the solvent was evaporated under reduce pressure. When necessary, the products were purified using silica gel chromatography with CH_2Cl_2/methanol (20:5, v/v) as the mobile phase. This protocol was used for the synthesis of 9*H*-fluoren-9-yl-piperazines **4b**, **4f-g**, **4j** and 1-(diphenylmethyl)-piperazines **10c** and **10f**.

Method iii: Pyridine-4-carboxylic acid (0.5 mmol, 0.061 g) was reacted with a solution of HBTU (0.55 mmol, 0.208 g), TEA (2 mmol, 0.202 g), 1-(9*H*-fluoren-9-yl)-piperazine (**3**) (0.5 mmol, 0.125 g) in dry DMF (5 mL). The reaction mixture was stirred for 4 h at 45 °C. Subsequently, the solution was diluted with aqueous NaCl (5%, w/v, 15 mL) and extracted with ethyl acetate (3 x 15 mL). Finally, the organic layer was dried over anhydrous magnesium sulfate. The mixture was filtered, and the solvent was evaporated under reduce pressure. The product was purified using silica gel

chromatography with CH_3Cl/methanol (40:1, v/v) as the mobile phase. This protocol was used for the synthesis of 9*H*-fluoren-9-yl-piperazine **4k**.

*4.2.1. (4-(9H-Fluoren-9-yl)piperazin-1-yl)(phenyl)methanone (**2**)*

Yellow powder; yield: 0.148 g (42%); m.p. 206-208 °C; ^{1}H NMR (60 MHz, $CDCl_3$): δ 2.63 (m, 4H, CH_2), 3.52 (br, 4H, CH_2), 4.84 (s, 1H, CH), 7.32-7.74 (m, 13H, Ar); ^{13}C NMR (100 MHz, $CDCl_3$): δ 48.3, 67.9, 120.7, 127.2, 128.6, 128.7, 130.6, 131.2, 133.6, 134.4, 142.1, 170.2; FTIR (UATR, cm^{-1}): 3330, 2930, 2817, 1634, 1447, 1425, 740; HRMS (ESI) calcd for $C_{24}H_{22}N_2O_3$ + H: 355.1805, found: 355.1796 $(M + H)^+$.

*4.2.2. (4-(9H-Fluoren-9-yl)piperazin-1-yl)(4-methoxyphenyl)methanone (**4a**)*

Brown powder; yield: 0.309 g (87%); m.p. 143-145 °C; ^{1}H NMR (60 MHz, $CDCl_3$): δ 2.59 -2.70 (m, 4H, CH_2), 3.55-3.71 (m, 4H, CH_2), 3.77 (s, 3H, OCH_3), 4.84 (s, 1H, CH), 6.82 (d, 2H, Ar), 7.25-7.78 (m, 10H, Ar); FTIR (UATR, cm^{-1}): 2931, 2798, 1632, 1424, 1250, 738; HRMS (ESI) calcd for $C_{25}H_{24}N_2O_2$ + H: 385.1911, found: 385.1900 $(M + H)^+$.

*4.2.3. (4-(9H-Fluoren-9-yl)piperazin-1-yl)(4-tolyl)methanone (**4b**)*

White powder; yield: 0.202 g (55%); m.p. 146-147 °C; ^{1}H NMR (60 MHz, $CDCl_3$): δ 2.33 (s, 3H, CH_3), 2.25-2.67 (m, 4H, CH_2), 3.53-3.64 (m, 4H, CH_2), 4.86 (s, 1H, CH), 7.20-7.675 (m, 14H, Ar); FTIR (UATR, cm^{-1}): 2920, 2795, 1624, 1429, 1269, 1005, 828, 742; HRMS (ESI) calcd for $C_{25}H_{24}N_2O$ + H: 369.1961, found: 369.1960 $(M + H)^+$.

*4.2.4. (4-(9H-Fluoren-9-yl)piperazin-1-yl)(4-chlorophenyl)methanone (**4c**)*

White powder; yield: 0.027 g (7%); m.p. 133-135 °C; ^{1}H NMR (60 MHz, $CDCl_3$): δ 2.60-2.71 (m, 4H, CH_2), 3.54-3.62 (m, 4H, CH_2), 4.86 (s, 1H, CH), 7.25-7.76 (m, 12H,

Ar); FTIR (UATR, cm^{-1}): 2808, 1624, 1431, 1269, 1004, 836, 740, 730; HRMS (ESI) calcd for $C_{24}H_{21}ClN_2O$ + H: 389.1410, found: 389.1415 $(M + H)^+$.

*4.2.5. (4-(9H-Fluoren-9-yl)piperazin-1-yl)(4-fluorophenyl)methanone (**4d**)*

Yellow powder; yield: 0.029 g (8%); m.p. 140-142 °C; ^1H NMR (60 MHz, $CDCl_3$): δ 2.57-2.71 (m, 4H, CH_2), 3.47-3.61 (m, 4H, CH_2), 4.86 (s, 1H, CH), 6.84-7.75 (m, 12H, Ar); FTIR (UATR, cm^{-1}): 2806, 1625, 1603, 1218, 1149, 1003, 840, 739; HRMS (ESI) calcd for $C_{24}H_{21}N_2OF$ + H: 373.1711, found: 373.1732 $(M + H)^+$.

*4.2.6. (4-(9H-Fluoren-9-yl)piperazin-1-yl)(4-nitrophenyl)methanone (**4e**)*

Yellow powder; yield: 0.095 g (24%); m.p. 119-120 °C; ^1H NMR (60 MHz, $CDCl_3$): δ 2.52-2.73 (m, 4H, CH_2), 3.29-3.71 (m, 4H, CH_2), 4.86 (s, 1H, CH), 7.25-7.76 (m, 10H, Ar), 8.21 (d, 2H, Ar); FTIR (UATR, cm^{-1}): 3330, 2931, 1630, 1599, 1516, 1439, 740; HRMS (ESI) calcd for $C_{24}H_{21}N_3O_3$ + H: 400.1656, found: 400.1644 $(M + H)^+$.

*4.2.7 (4-(9H-Fluoren-9-yl)piperazin-1-yl)(3-tolyl)methanone (**4f**)*

Yellow powder; yield: 0.0856 (77%); m.p. 124-126 °C; ^1H NMR (60 MHz, $CDCl_3$): δ 2.32 (s, 3H, CH_3), 2.71 (br, 4H, CH_2), 3.62 (br, 4H, CH_2), 4.94 (s, 1H, CH), 7.16-7.841 (m, 12H, Ar); FTIR (UATR, cm^{-1}): 3373, 293, 2808, 1632, 1450, 1421, 1275, 1201, 1005, 810, 737; HRMS (ESI) calcd for $C_{25}H_{24}N_2O$ + H: 369.1961, found: 369.1960 $(M + H)^+$.

*4.2.8. (4-(9H-Fluoren-9-yl)piperazin-1-yl)(2-tolyl)methanone (**4g**)*

Yellow powder; yield: 0.0917 (83%); m.p. 63-64 °C; ^1H NMR (60 MHz, $CDCl_3$): δ 2.24 (s, 3H, CH_3), 2.54 (br, 2H, CH_2), 2.91 (br, 2H, CH_2), 3.28 (br, 2H, CH_2), 3.89 (br, 2H, CH_2), 5.96 (s, 1H, CH), 7.16-7.77 (m, 12H, Ar); FTIR (UATR, cm^{-1}): 2923, 2817, 1627,

1426, 1255, 1001, 729; HRMS (ESI) calcd for $C_{25}H_{24}N_2O$ + H: 369.1691, found: 369.1966 $(M + H)^+$.

*4.2.9. (4-(9H-Fluoren-9-yl)piperazin-1-yl)(3-fluorophenyl)methanone (**4h**)*

Brown powder; yield: 0.029 g (8%); m.p. 165-167 °C; ^{1}H NMR (60 MHz, $CDCl_3$): δ 2.53-2.69 (m, 4H, CH_2), 3.41-3.66 (m, 4H, CH_2), 4.85 (s, 1H, CH), 6.99-7.78 (m, 13H, Ar); FTIR (UATR, cm^{-1}): 3063, 2824, 1639, 1582, 1439, 1277, 1004, 740; HRMS (ESI) calcd for $C_{24}H_{21}FN_2O$ + H: 373.1773, found: 373.1747 $(M + H)^+$.

*4.2.10. (4-(9H-Fluoren-9-yl)piperazin-1-yl)(2-fluorophenyl)methanone (**4i**)*

White powder; yield: 0.119 g (32%); m.p. 169-171 °C; ^{1}H NMR (60 MHz, $CDCl_3$): δ 2.37-2.53 (m, 2H, CH_2), 2.71-2.85 (m, 2H, CH_2), 3.18-3.34 (m, 2H, CH_2), 3.70-3.90 (m, 2H, CH_2), 4.85 (s, 1H, CH), 6.99-7.76 (m, 12H, Ar); FTIR (UATR, cm^{-1}): 3342, 2835, 1631, 1610, 1451, 1431, 1276, 1007, 741; HRMS (ESI) calcd for $C_{24}H_{21}FN_2O$ + H: 373.1773, found: 373.1747 $(M + H)^+$.

*4.2.11. (4-(9H-Fluoren-9-yl)piperazin-1-yl)(2,5-difluorophenyl)methanone (**4j**)*

White powder; yield: 0.339 g (87%); m.p. 167-168 °C; ^{1}H NMR (60 MHz, $CDCl_3$): δ 2.64-2.99 (m, 4H, CH_2), 3.41-3.59 (m, 2H, CH_2), 3.89-4.04 (m, 2H, CH_2), 5.10 (s, 1H, CH), 6.93-7.87 (m, 11H, Ar); ^{13}C NMR (100 MHz, $CDCl_3$): δ 48.6, 69.2, 115.8 (dd, J = 25.2, J = 8.4), 117.0 (dd, J = 24.4, J = 8.4), 118.1 (dd, J = 24.0, J = 8.8), 120.1, 126.5, 127.6, 129.2, 141.3, 153.9 (d, J = 244.9), 158.6 (d, J = 244.9), 163.6; FTIR (UATR, cm^{-1}): 3061, 2929, 1634, 1611, 1449, 1008, 737; HRMS (ESI) calcd for $C_{24}H_{20}F_2N_2O_3$ + H: 391.1616, found: 391.1616 $(M + H)^+$.

*4.2.12. (4-(9H-fluoren-9-yl)piperazin-1-yl)(pyridin-4-yl)methanone (**4k**)*

White powder; yield: 0.148 g (83%); m.p. 156-157 °C; ^{1}H NMR (400 MHz, $CDCl_3$): δ 2.42-2.44 (m, 2H, CH_2), 2.83-2.85 (m, 2H, CH_2), 3.27-3.29 (m, 2H, CH_2), 3.78-3.80 (m, 2H, CH_2), 4.87 (s, 1H, CH), 7.23 (d, *J* = 6.3, 2H, Ar), 7.30 (t, *J* = 7.8, 2H, Ar) 7.39 (t, *J* = 7.4, 2H, Ar), 7.60 (d, *J* = 7.4, 2H, Ar), 7.69 (d, *J* = 7.4, 2H, Ar), 8.63 (d, *J* = 5.9, 2H, Ar). ^{13}C NMR (100 MHz, $CDCl_3$): δ 42.8, 48.2, 48.5, 49.4, 69.8, 119.9, 121.2, 125.8, 127.2, 128.4, 141.0, 143.1, 143.4, 150.1, 167.6; FTIR (UATR, cm^{-1}): 2815, 1636, 1440, 1279, 1000, 832, 751; HRMS (ESI) calcd for $C_{23}H_{21}N_3O$ + H: 356.1757, found: 356.1756 $(M + H)^+$.

*4.2.13. (4-Benzhydrylpiperazin-1-yl)(phenyl)methanone (**10a**)*

White powder; yield: 0.309 g (87%); m.p. 145-146 °C; ^{1}H NMR (60 MHz, $CDCl_3$): δ 2.33-2.47 (m, 4H, CH_2), 3.47-3.68 (m, 4H, CH_2), 4.26 (s, 1H, CH), 7.61-7.35 (m, 15H, Ar); FTIR (UATR, cm^{-1}): 3024, 2808, 1631, 1446, 1265, 996, 706; HRMS (ESI) calcd for $C_{24}H_{24}N_2O$ + H: 357.1961, found: 357.1937 $(M + H)^+$.

*4.2.14. (4-Benzhydrylpiperazin-1-yl)(4-methoxyphenyl)methanone (**10b**)*

White powder; yield: 0.142 g (37%); m.p. 64-66 °C; ^{1}H NMR (60 MHz, $CDCl_3$): δ 2.34-2.49 (m, 4H, CH_2), 3.63-3.63 (m, 4H, CH_2), 3.78 (s, 3H, OCH_3), 5.27 (s, 1H, CH), 6.78-6.92 (d, 2H, Ar), 7.21-7.43 (m, 12H, C_5H_6); FTIR (UATR, cm^{-1}): 3421, 2808, 1605, 1427, 1230, 996, 704; HRMS (ESI) calcd for $C_{25}H_{26}N_2O$ + H: 387.2120, found: 387.2146 $(M + H)^+$.

*4.2.15. (4-Benzhydrylpiperazin-1-yl)(4-tolyl)methanone (**10c**)*

White powder; yield: 0.203 g (55%); m.p. 62-64 °C; ^{1}H NMR (60 MHz, $CDCl_3$): δ 2.33 (s, 3H, CH_3), 2.35-2.49 (m, 4H, CH_2), 3.73-3.79 (m, 4H, CH_2), 4.36 (s, H, CH), 7.20-

7.47 (m, 14H, Ar); FTIR (UATR, cm^{-1}): 2807, 1627, 1426, 1285, 1253, 996, 748, 705; HRMS (ESI) calcd for $C_{27}H_{28}N_2O_2$ + H: 371.2118, found: 371.2131 $(M + H)^+$.

*4.2.16. (4-Benzhydrylpiperazin-1-yl)(4-chlorophenyl)methanone (**10d**)*

Brown powder; yield: 0.234 g (60%); m.p. 130-132 °C; ^1H NMR (60 MHz, $CDCl_3$): δ 2.36–2.51 (m, 4H, CH_2), 3.53–3.78 (m, 4H, CH_2), 4.28 (s, 1H, CH), 7.26-7.45 (m, 15H, Ar); FTIR (UATR, cm^{-1}): 3027, 2808, 1629, 1431, 1254, 1087, 996, 832, 745, 696; HRMS (ESI) calcd for $C_{24}H_{23}ClN_2O$ + H: 391.1572, found: 391.1609 $(M + H)^+$.

*4.2.17. (4-Benzhydrylpiperazin-1-yl)(4-fluorophenyl)methanone (**10e**)*

Brown powder; yield: 0.202 g (54%); m.p. 54-57 °C; ^1H NMR (60 MHz, $CDCl_3$): δ 2.42-2.52 (m, 4H, CH_2), 2.92–3.06 (m, 2H, CH_2), 3.36-3.60 (m, 2H, CH_2), 4.24 (s, 1H, CH), 6.88-7.51 (m, 14H, Ar); FTIR (UATR, cm^{-1}): 2811, 1628, 1603, 1451, 1432, 1254, 1223, 996, 843, 705; HRMS (ESI) calcd for $C_{24}H_{23}N_2OF$ + H: 375.1867, found: 372.1874 $(M + H)^+$.

*4.2.18. (4-Benzhydrylpiperazin-1-yl)(2,5-difluorophenyl)methanone (**10f**)*

White powder; yield: 0.321 g (82%); m.p. 78-79 °C; ^1H NMR (60 MHz, $CDCl_3$): δ 2.28-2.52 (br, 4H, CH_2), 3.25-3.41 (m, 2H, CH_2), 3.70-3.88 (m, 2H, CH_2), 4.26 (s, 1H, CH), 6.93-7.41 (m, 13H, Ar); FTIR (UATR, cm^{-1}): 2919, 1627, 1427, 1286, 1253, 996, 705; HRMS (ESI) calcd for $C_{24}H_{22}F_2N_2O$ + H: 393.1773, found: 393.1747 $(M + H)^+$.

*4.3. General procedure for the synthesis of piperazines **5a-b** and **11***

Sulfonyl halide (1.2 mmol) was dissolved in dry CH_2Cl_2 (5 mL), and the resultant solution was cooled to 0 °C. To this solution, TEA (2.2 mmol, 0.222 g), 1-(9*H*-fluoren-

9-yl)-piperazine (**3**) (1.1 mmol, 0.275 g) or 1-(diphenylmethyl)-piperazine (**9**) (1.1 mmol, 0.277 g), in dry CH_2Cl_2 (5 mL) was added dropwise. After the addition, the reaction mixture was stirred for 16 h at room temperature. Extraction and purification were performed as previously described for piperazines **2**, **4** and **10**.

*4.3.1. 1-(9H-Fluoren-9-yl)-4-(phenylsulfonyl)piperazine (**5a**)*

White powder; yield: 0.238 g (61%); m.p. 152-154 °C; ^{1}H NMR (60 MHz, $CDCl_3$): δ 2.58-2.70 (m, 4H, CH_2), 2.85-3.11 (m, 4H, CH_2), 4.91 (s, 1H, CH), 7.13-7.89 (m, 13H, Ar); FTIR (UATR, cm^{-1}): 3418, 2887, 2835, 1634, 1348, 1171, 735; HRMS (ESI) calcd for $C_{23}H_{22}N_2O_2S$ + H: 391.1475, found: 391.1467 $(M + H)^+$.

*4.3.2. 1-(9H-Fluoren-9-yl)-4-(o-tolylsulfonyl)piperazine (**5b**)*

White powder; yield: 0.331 g (82%); m.p. 68-70 °C; ^{1}H NMR (60 MHz, $CDCl_3$): δ 2.61-2.74 (m, 7H, CH_2), 3.09–3.24 (m, 4H, CH_2), 4.81 (s, 1H, CH), 7.49-7.75 (m, 13H, Ar); FTIR (UATR, cm^{-1}): 1447, 1314, 1158, 1133, 940, 722; HRMS (ESI) calcd for $C_{24}H_{24}N_2O_2S$ + H: 405.1631, found: 405.1631 $(M + H)^+$.

*4.3.3. 1-Benzhydryl-4-(phenylsulfonyl)piperazine (**11**)*

White powder; yield: 0.058 (15%); m.p. 153-155 °C (m.p. 157-159 °C [49]); ^{1}H NMR (60 MHz, $CDCl_3$): δ 2.43-2.50 (m, 4H, CH_2), 3.03-3.63 (m, 4H, CH_2), 4.24 (s, 1H, CH), 7.25-7.83 (m, 15H, Ar); FTIR (UATR, cm^{-1}): 2855, 2811, 1447, 1347, 1331, 1169, 944, 741, 689; HRMS (ESI) calcd for $C_{25}H_{26}N_2O_2S$ + H: 393.1631, found: 393.1607 $(M + H)^+$.

*4.4. General procedure for the synthesis of piperazines **6** and **12***

The cinnamic acid precursor was synthesized as previously described [28]. Thereafter, this acid (1 mmol, 0.148 g) was reacted with a solution of thionyl chloride in CH_2Cl_2 (1 M, 6 mL) for 5 h in refluxing toluene (5 mL). The obtained acyl chloride was dissolved in dry CH_2Cl_2 (5 mL), and the resultant solution was cooled to 0 °C. To this solution, TEA (4.4 mmol, 0.444 g), 1-(9*H*-fluoren-9-yl)-piperazine (**3**) (1.1 mmol, 0.275 g) or 1-(diphenylmethyl)-piperazine (**9**) (1.1 mmol, 0.277 g) in dry CH_2Cl_2 (5 mL) was added dropwise. After the addition, the reaction mixture was stirred for 16 h at room temperature. Finally, ethyl ether (15 mL) was added to the reaction mixture, and the precipitate was isolated on a filter. The products were purified using silica gel chromatography with CH_2Cl_2/methanol (20:5, v/v) as the mobile phase.

*4.4.1. (E)-1-(4-(9H-Fluoren-9-yl)piperazin-1-yl)-3-phenylprop-2-en-1-one (**6**)*

White powder; yield: 0.098 g (26%); m.p. 169-170 °C; ^{1}H NMR (60 MHz, $CDCl_3$): δ 2.34-2.50 (m, 4H, CH_2), 3.61-3.75 (m, 4H, CH_2), 4.86 (s, 1H, CH), 6.77 (d, J = 15 Hz, 1H, CH_{trans}), 7.25-7.53 (m, 17H, Ar), 7.77 (d, J = 15, CH_{trans}); FTIR (UATR, cm^{-1}): 3060, 2813, 1649, 1605, 1410, 1202, 740; HRMS (ESI) calcd for $C_{26}H_{24}N_2O$ + H: 381.1961, found: 381.1967 $(M + H)^+$.

*4.4.2. (E)-1-(4-Benzhydrylpiperazin-1-yl)-3-phenylprop-2-en-1-one (**12**)*

White powder; yield: 0.126 g (33%); m.p. 141-143 °C; ^{1}H NMR (60 MHz, $CDCl_3$): δ 2.34-2.50 (m, 4H, CH_2), 3.61-3.75 (m, 4H, CH_2), 4.26 (s, 1H, CH), 6.80 (d, J = 15 Hz, 1H, CH_{trans}), 7.17-7.36 (m, 18H, Ar), 7.66 (d, J = 15 Hz, 1H, CH_{trans}); FTIR (UATR, cm^{-1}): 3023, 2809, 1644, 1595, 1452, 1439, 1229, 705; HRMS (ESI) calcd for $C_{26}H_{26}N_2O$ + H: 383.2123, found: 383.2118 $(M + H)^+$.

*4.5. General procedure for the synthesis of 9H-fluoren-9-yl-piperazine **7***

Bromo-*N*-phenylacetamide was synthesized from 2-bromoacetyl chloride and aniline as previously described [29]. A solution containing bromo-*N*-phenylacetamide (1.04 mmol, 0.221 g), potassium carbonate (3.12 mmol, 1.08 g), and 1-(9*H*-fluoren-9-yl)-piperazine (**3**) (1.1 mmol, 0.275 g) in DMF (8 mL) was stirred under argon atmosphere for 24 h at room temperature. Thereafter, the solution was diluted with distilled water (50 mL). The obtained solid was isolated on a filter and dried under reduce pressure. The product was purified using silica gel chromatography with chloroform/methanol (50:50, v/v) as the mobile phase.

*4.5.1. 2-(4-(9H-Fluoren-9-yl)piperazin-1-yl)-N-phenylacetamide (**7**)*

White powder; yield: 0.172 g (51%); m.p. 174-175 °C; ^{1}H NMR (60 MHz, $CDCl_3$): δ 2.60-2.75 (m, 8H, CH_2), 3.10 (s, 2H, CH_2), 4.86 (s, 1H, CH), 7.03-7.78 (m, 15H, Ar); FTIR (UATR, cm^{-1}): 2546, 1682, 1447, 1313, 1133, 952, 736; HRMS (ESI) calcd for $C_{25}H_{25}N_3O$ + H: 384.2048, found: 384.2070 $(M + H)^+$.

*4.6. General procedure for the synthesis of 9H-fluoren-9-yl-piperazine **8***

A solution containing (bromomethyl)benzene (1.04 mmol, 0.124 mL), potassium carbonate (3.12 mmol, 1.08 g), and 1-(9*H*-fluoren-9-yl)-piperazine (**3**) (1.1 mmol, 0.275 g) in DMF (8 mL) was stirred under argon atmosphere and at room temperature for 24 h. Thereafter, the mixture was diluted with distilled water (20 mL). The obtained solid was isolated on a filter and dried under reduce pressure. The product was purified using silica gel chromatography with chloroform/methanol (50:50, v/v) as the mobile phase.

*4.6.1. 9-(4-Benzylcyclohexyl)-9H-fluorene (**8**)*

Yellow powder; yield: 0,055 g (55%); m.p. 129-131 °C; ^{1}H NMR (60 MHz, $CDCl_3$): δ 2.38 (br, 8H, CH_2), 3.48 (s, 2H, CH_2), 4.82 (s, 1H, CH), 7.62-7.73 (m, 15H, Ar); FTIR

(UATR, cm^{-1}): 2807, 1449, 1130, 1007, 736, 697; HRMS (ESI) calcd for $C_{24}H_{24}N_2$ + H: 341.2012, found: 341.2016 $(M + H)^+$.

4.7. Theoretical Calculations and docking simulations

The geometry of the compound was optimized using semi-empirical AM1 and PM3 methods implemented in the HyperChem 7.52 package (2002) [50]. The structures were fully optimized without fixing any parameter, thus, bringing all geometric variables to their equilibrium values. The energy minimization protocol employed the Polak-Ribiere conjugated gradient algorithm. Convergence to a local minimum was achieved when the energy gradient was ≤ 0.01 $kcal \cdot mol^{-1}$. The RHF method was used in the spin pairing for the two semi-empirical tools.

Flexible ligand docking, carried out using AutoDock4.2.5.1 and AutoDockTools4 software [51-52], employed the crystal structure of the piperazine **1** (Genz-10850) bound to *Mt*InhA (PDB ID: 1P44). The NADH coenzyme was treated as part of the protein receptor in all docking simulations. Water molecules were removed, polar hydrogens were added, and Gasteiger partial atomic charges for ligands were assigned by AutoDockTools4 [51]. For the docking simulation, the active site was set on a cubic grid, spaced at 0.375 Å, with dimensions of 60 points × 60 points × 60 points centered on the crystallographic bound ligand **1**. This grid is large enough to include the NADH coenzyme as part of the protein receptor, as well as the *Mt*InhA substrate binding pocket in 1P44. The results of each docking experiment were derived from 25 independent runs, for which a maximum number of 27,000 LGA (Lamarckian Genetic Algorithm) generations was generated on the initial population of 150 individuals, a maximum number of 2.5 x 10^6 energy evaluations, with an elitism value of 1, a

mutation rate of 0.02, and a cross-over rate of 0.8. For the local search, the pseudo-Solis and Wets method was applied using default parameters [52]. Each run provides one predicted binding mode. At the end of the docking experiment, binding modes with root-mean-square deviation (RMSD) of 2.0 Å within each other and to the crystallographic bound ligand **1** were placed in the same cluster.

4.8. Enzymatic activity assays

4.8.1. Inhibition assessed by steady-state kinetics measurements

The expression and purification of recombinant *Mt*InhA were performed as previously described [36-37]. The substrate DD-CoA was synthesized from 2-*trans*-dodecenoic acid and coenzyme A via anhydride formation following acylation, as previously described [36]. DD-CoA was purified by reverse-phase HPLC using a 19 x 300 mm C_{18} μBondapak column (Waters Associates, Milford, MA) as previously described [53]. Protein concentration was determined by the Bradford method [54] using serum albumin as the standard.

The steady-state velocities in the presence of the synthesized compounds were determined using a UV-2550 UV/visible spectrophotometer (Shimadzu) by monitoring NADH oxidation to NAD^+ at 340 nm ($\varepsilon_{\beta\text{-NADH}} = 6.22\ M^{-1}\ cm^{-1}$) due the reduction of the DD-CoA substrate. Experiments were performed at 25 °C in 100 mM PIPES, pH 7.0, and measurement of the enzyme-catalyzed reaction started with the addition of *Mt*InhA at 2.2 μM to the assay mixture (500 μL final volume) and data collected for 1 min.

4.8.2. IC_{50} determinations

The IC_{50} values were determined by adding different concentrations of the compounds (dissolved in DMSO) to the reaction mixture, and the enzyme velocity was used to determine the % inhibition. As a control, the maximal rate of the enzymatic reaction (100% *Mt*InhA activity) was determined in the absence of inhibitor and in the presence of fixed non-saturating concentrations of NADH ($K_m \cong 60$ μM) and DD-CoA ($K_m \cong 45$ μM), in the presence of 1% DMSO [36-37]. The IC_{50} values were estimated using equation 1, where [*I*] is the inhibitor concentration, v_i is the initial velocity in the presence of the inhibitor, v_o is the initial velocity in the absence of inhibitor, and the IC_{50} value is defined as the concentration of the inhibitor that reduces the enzyme velocity by half.

$$\frac{v_i}{v_0} = \frac{1}{1+\left(\frac{[I]}{IC_{50}}\right)} \qquad \text{Eq. (1)}$$

4.8.3. Time-dependent inhibition

To evaluate whether or not enzyme inhibition may be time dependent, 2.2 μM recombinant *Mt*InhA was preincubated with 0.2 μM inhibitor (final concentration), which was then added at different times (up to 30 min) to the reaction mixture, as previously described. The change in the initial velocity as a function of time was monitored, and the percent inhibition was determined. This analysis was performed to determine if inhibition follows a rapid equilibrium mode (classical competitive, uncompetitive and noncompetitive inhibition) or if there is a slow step in the

equilibrium process. Control experiments were also carried out to evaluate whether or not DMSO may have any inhibitory effect on *Mt*InhA at the maximum concentration (1%). For these experiments, identical concentrations of recombinant *Mt*InhA and inhibitor were preincubated with 0.1 μM NADH (final concentration), 0.1 μM DD-CoA (final concentration) or 1% DMSO (final concentration) [20].

4.8.4. Mode of inhibition and determination of the overall inhibition constant

The compounds that exhibited IC_{50} values below 3 μM were analyzed for the mode of inhibition and overall inhibition constants (K_i). Lineweaver-Burk (double-reciprocal) plots were employed to determine the mode of inhibition (competitive, noncompetitive or uncompetitive) and data fitting to appropriate equations gave values for the inhibition constants (K_{is} and/or K_{ii}). In short, the inhibition mode was proposed based on the effects on V_{max} and K_m values for each inhibition type, resulting in plots with distinct straight line patterns toward either NADH or DD-CoA as follows: lines intercept on *y* axis for competitive inhibition (does not affect the apparent V_{max} and increases apparent K_m), lines intercept on left of *y* axis for noncompetitive inhibition (decreases apparent V_{max}, and does not affect apparent K_m values if $K_{is} = K_{ii}$, increases the apparent K_m values if $K_{is} < K_{ii}$, or decreases the K_m values if $K_{is} > K_{ii}$), and parallel lines for uncompetitive inhibition (decreases both apparent V_{max} and K_m values) [44]. Initial rates were measured at varying NADH concentrations (10, 20, 40, 60, 100, and 160 μM) at fixed non-saturating DD-CoA concentrations ($K_m \cong 45$ μM), and fixed-varied inhibitor concentrations (0.05–4 μM). The K_i values with respect to NADH were calculated by fitting the data to an equation that describes uncompetitive inhibition (Eq. 2), in which [*I*] is the inhibitor concentration, [*S*] is the substrate concentration, K_m is the Michaelis

constant, V_{max} is the maximal velocity, and K_{ii} is the overall inhibition constant for the ESI complex [44].

$$\frac{1}{v_0} = \frac{K_m}{V_{max}}\left(\frac{1}{[S]}\right) + \frac{1}{V_{max}}\left(1 + \frac{[I]}{K_{ii}}\right) \quad \text{Eq. (2)}$$

Initial rates were measured as a function of DD-CoA concentration (15, 30, 45, 75, 105, and 135 μM) at fixed non-saturating NADH concentrations ($K_m \cong 60$ μM) and fixed-varied inhibitor concentrations (0.05-4 μM). The K_i values with respect to the DD-CoA substrate were calculated by fitting the data to an equation that describes noncompetitive (Eq. 3) or competitive (Eq. 4) inhibition, in which [*I*] is the inhibitor concentration, [*S*] is the substrate concentration, K_m is the Michaelis constant, V_{max} is the maximal velocity, K_{ii} is the overall inhibition constant for the ESI complex, and K_{is} is the overall inhibition constant for the EI complex [44].

$$\frac{1}{v_0} = \frac{K_m}{V_{max}}\left(1 + \frac{I}{K_{is}}\right)\left(\frac{1}{[S]}\right) + \frac{1}{V_{max}}\left(1 + \frac{[I]}{K_{ii}}\right) \quad \text{Eq. (3)}$$

$$\frac{1}{v_0} = \frac{K_m}{V_{max}}\left(1 + \frac{I}{K_{is}}\right)\left(\frac{1}{[S]}\right) + \frac{1}{V_{max}} \quad \text{Eq. (4)}$$

An independent experiment was performed using compound **2**. Initial rates were measured as a function of the NADH concentration (10-120 μM) at a fixed saturating

DD-CoA concentration (135 µM), and fixed-varied inhibitor concentrations (0, 0.100, 0.250, and 0.450 µM). The K_i values with respect to NADH were calculated by fitting the data to an equation that describes uncompetitive inhibition (Eq. 2). Initial rates were measured as a function of the DD-CoA concentration (15-200 µM), fixed saturating NADH concentration (240 µM), and fixed-varied inhibitor concentrations (0, 0.05, 0.150, and 0.450 µM). The K_i values with respect to the DD-CoA substrate were calculated by fitting the data to an equation describing competitive inhibition (Eq. 4). Higher concentrations of DD-CoA could not be used because increasing the concentration above 135 µM resulted in a decrease in the rate, possibly due to substrate inhibition [37]. For all K_i determinations, each initial velocity was determined in duplicate, and at least five different substrate concentrations were examined.

Supporting Information

^{1}H and ^{13}C NMR spectra of compounds **2** and **4j**; Lineweaver-Burk plots of compounds **2**, **4a-d**, **4f** and **4h-j**; crystal data and details of the data collection and structure refinement; select experimentally determined and calculated geometric parameters using the AM1 and PM3 methods for **4d**; MIC determination for the most potent *Mt*InhA inhibitors. This material is available free of charge and can be obtained via the Internet.

Acknowledgments

This work was supported by funds from the National Institute of Science and Technology on Tuberculosis (INCT-TB), Decit/SCTIE/MS-MCT-CNPq-FNDCT-CAPES (Brazil) to D. S. Santos and L. A. Basso. O. N. Souza (CNPq, 305984/2012-8), D. S. Santos (CNPq, 304051/1975-06), and L. A. Basso (CNPq, 520182/99-5) are

Research Career Awardees of the National Research Council of Brazil (CNPq). The fellowships from CNPq (M. Rotta, K. Pissinate, and L.F.S.M. Timers), CAPES (A. D. Villela), and FAPERGS/CAPES (J. F. R. Bachega) are also acknowledged.

References and notes

[1] World Health Organization, 2013. Global tuberculosis report 2013.

[2] Gandhi, N. R.; Nunn, P.; Dheda, K.; Schaaf, H. S.; Zignol, M.; van, Soolingen, D.; Jensen, P.; Bayona, J. Multidrug-resistant and extensively drug-resistant tuberculosis: a threat to global control of tuberculosis, **Lancet**, v. 375, n. 9728, 2010, p. 1830-1843.

[3] Zhang, Y.; Yew, W. W.; Barer, M. R. Targeting persisters for tuberculosis control, **Antimicrob Agents Chemother.**, v. 56, n. 5, 2012, p. 2223-2230.

[4] Zumla, A.; Nahid, P.; Cole, S. T. Advances in the development of new tuberculosis drugs and treatment regimens, **Nat. Rev. Drug Discov.**, v. 12, n. 5, 2013, p. 388-404.

[5] Palomino, J. C.; Martin, A. TMC207 becomes bedaquiline, a new anti-TB drug, **Future Microbiol.**, v. 8, n. 9, 2013, p. 1071-1080.

[6] Avorn, J. Approval of a tuberculosis drug based on a paradoxical surrogate measure, **JAMA-J. Am. Med. Assoc.**, v. 309, n. 13, 2013, p. 1349-1350.

[7] Lu, H.; Tonge, P. J. Inhibitors of FabI, an enzyme drug target in the bacterial fatty acid biosynthesis pathway, **Accounts Chem. Res.**, v. 41, n. 1, 2008, p. 11-20.

[8] Brennan, P. J.; Nikaido, H. The envelope of mycobacteria, **Annu. Rev. Biochem**, v. 64, 1995, p. 29-63.

[9] Takayama, K.; Wang, C.; Besra, G. S. Pathway to synthesis and processing of mycolic acids in *Mycobacterium tuberculosis*, **Clin. Microbiol. Rev**., v. 18, n. 1, 2005, p. 81-101.

[10] Barry, C. E. III; Lee, R. E.; Mdluli, K.; Sampson, A. E.; Schroeder, B. G.; Slayden, R. A.; Yuan, Y. Mycolic acids: Structure, biosynthesis and physiological functions, **Prog. Lipid. Res.**, v. 37, n. 2-3, 1998, p. 143-179.

[11] Schroeder, E. K.; de Souza, O. N.; Santos, D. S.; Blanchard, J. S.; Basso, L. A. Drugs that inhibit mycolic acid biosynthesis in *Mycobacterium tuberculosis*, **Curr. Pharm. Biotechnol.**, v. 3, n. 3, 2002, p. 197-225.

[12] Banerjee, A.; Dubnau, E.; Quémard, A.; Balasubramanian, V.; Um, K. S.; Wilson, T.; Collins, D.; de Lisle, G.; Jacobs, W. R. Jr. *inhA*, a gene encoding a target for isoniazid and ethionamide in *Mycobacterium tuberculosis*, **Science**, v. 263, n. 5144, 1994, p. 227-230.

[13] Rozwarski, D. A.; Grant, G. A.; Barton, D. H.; Jacobs, W. R. Jr.; Sacchettini, J. C. Modification of the NADH of the isoniazid target (InhA) from *Mycobacterium tuberculosis*, **Science**, v. 279, n. 5347, 1998, p. 98-102.

[14] Vilchèze, C.; Wang, F.; Arai, M.; Hazbón, M. H.; Colangeli, R.; Kremer, L.; Weisbrod, T. R.; Alland, D.; Sacchettini, J. C.; Jacobs, W. R. Jr. Transfer of a point mutation in *Mycobacterium tuberculosis inhA* resolved the target of isoniazid, **Nat. Med.**, v. 12, n. 9, 2006, p. 1027-1029.

[15] Johnsson, K.; Schultz, P. G. Mechanistic studies of the oxidation of isoniazid by the catalase peroxidase from *Mycobacterium tuberculosis*, **J. Am. Chem. Soc.**, v. 116, n. 16, 1994, p. 7425-7426.

[16] Lei, B.; Wei, C. J.; Tu, S. C. Action mechanism of antitubercular isoniazid: Activation by *Mycobacterium tuberculosis* KatG, isolation, and characterization of InhA inhibitor, **J. Biol. Chem.**, v. 275, n. 4, 2000, p. 2520-2526.

[17] Rawat, R.; Whitty, A.; Tonge, P. J. The isoniazid-NAD adduct is a slow, tight-binding inhibitor of InhA, the *Mycobacterium tuberculosis* enoyl reductase: Adduct affinity and drug resistance, **P. Natl. Acad. Sci. U.S.A.**, v. 100, n. 24, 2003, p. 13881-13886.

[18] Zhang, Y.; Heym, B.; Allen, B.; Young, D.; Cole, S. The catalase-peroxidase gene and isoniazid resistance of *Mycobacterium tuberculosis*, **Nature**, v. 358, n. 6387, 1992, p. 591-593.

[19] Heym, B.; Honoré, N.; Truffot-Pernot, C.; Banerjee, A.; Schurra, C.; Jacobs W. R. Jr.; van Embden, J. D.; Grosset, J. H.; Cole, S. T. Implications of multidrug resistance for the future of short-course chemotherapy of tuberculosis: a molecular study, **Lancet**, v. 344, n. 8918, 1994, p. 293-298.

[20] Oliveira, J. S.; Sousa, E. H.; Basso, L. A.; Palaci, M.; Dietze, R.; Santos, D. S.; Moreira, I. S. An inorganic iron complex that inhibits wild-type and an isoniazid-resistant mutant 2-*trans*-enoyl-ACP (CoA) reductase from *Mycobacterium tuberculosis*, **Chem. Commun.**, v. 3, 2004, p. 312-313.

[21] Rodrigues-Junior, V. S.; dos Santos, A. Jr.; dos Santos, A. J.; Schneider, C. Z.; Calixto, J. B.; Sousa, E. H. S.; de França Lopes, L. G.; Souto, A. A.; Basso, L. A.; Santos, D. S.; Campos, M. M. Activity of IQG-607, a new orally active compound, in a murine model of *Mycobacterium tuberculosis* infection, **Int. J. Antimicrob. Ag.**, v. 40, n. 2, 2012, p. 182-185.

[22] Pauli, I.; dos Santos, R. N.; Rostirolla, D. C.; Martinelli, L. K.; Ducati, R. G.; Timmers, L. F. S. M.; Basso, L. A.; Santos, D. S.; Guido, R. V. C.; Andricopulo, A. D.; de Souza, O. N. Discovery of new inhibitors of *Mycobacterium tuberculosis* InhA enzyme using virtual screening and a 3D-pharmacophore-based approach, **J. Chem. Inf. Model.,** v. 53, n. 9, 2013, p. 2390–2401.

[23] Shirude, P. S.; Madhavapeddi, P.; Naik, M.; Murugan, K.; Shinde, V.; Nandishaiah, R.; Bhat, J.; Kumar, A.; Hameed, S.; Holdgate, G.; Davies, G.; McMiken, H.; Hegde, N.; Ambady, A.; Venkatraman, J.; Panda, M.; Bandodkar, B.; Sambandamurthy, V. K.; Read, J. A. Methyl-thiazoles: a novel mode of inhibition with the potential to develop novel inhibitors targeting InhA in *Mycobacterium tuberculosis*, **J. Med. Chem.** v. 56, n. 21, 2013, p. 8533-8542.

[24] He, X.; Alian, A.; Stroud, R.; Ortiz de Montellano, P. R. Pyrrolidine carboxamides as a novel class of inhibitors of enoyl acyl carrier protein reductase from *Mycobacterium tuberculosis*, **J. Med. Chem.,** v. 49, n. 21, 2006, p. 6308−6323.

[25] Kuo, M. R.; Morbidoni, H. R.; Alland, D.; Sneddon, S. F.; Gourlie, B. B.; Staveski, M. M.; Leonard, M.; Gregory, J. S.; Janjigian, A. D.; Yee, C.; Musser, J. M.; Kreiswirth, B.; Iwamoto, H.; Perozzo, R.; Jacobs, W. R. Jr.; Sacchettini, J. C.; Fidock, D. A. Targeting tuberculosis and malaria through inhibition of enoyl reductase: compound activity and structural data, **J. Biol. Chem.**, v. 278, n. 23, 2003, p. 20851-20859.

[26] He, X.; Alian, A.; Ortiz de Montellano, P. R. Inhibition of the *Mycobacterium tuberculosis* enoyl acyl carrier protein reductase InhA by arylamides, **Bioorg. Med. Chem.**, v. 15, n. 21, 2007, p. 6649-6658.

[27] Pan, P.; Tonge, P. J. Targeting InhA, the FASII enoyl-ACP reductase: SAR studies on novel inhibitor scaffolds, **Current Top. Med. Chem.**, v. 12, n. 7, 2012, p. 672-693.

[28] Misra, K.; Maity, H. S.; Chanda, S.; Nag, A. New greener alternatives for bioreduction of aromatic aldehydes and decarboxylation of aromatic acids using juice of fruits, **J. Mol. Catal. B-Enzym.**, v. 82, 2012, p. 92-95.

[29] Macpherson, I. S.; Kirubakaran, S.; Gorla, S. K.; Riera, T. V.; D'Aquino, J. A.; Zhang, M.; Cuny, G. D.; Hedstrom, L. The structural basis of Cryptosporidium-specific IMP dehydrogenase inhibitor selectivity, **J. Am. Chem. Soc.**, v. 132, n. 18, 2010, p. 1230-1231.

[30] Freire, E. Isothermal titration calorimetry: controlling binding forces in lead optimization, **Drug Discov. Today: Technol**, v. 1, n. 3, 2004, p. 295-299.

[31] CCDC number 1000538 contains the supplementary crystallographic data for compound reported in this paper. These data can be obtained free of charge via www.ccdc.cam.ac.uk/conts/retrieving.html (or from the Cambridge Crystallographic Data Centre, 12, Union Road, Cambridge CB2 1EZ, UK; fax: +44 1223 336033).

[32] Dewar, M. J. S.; Zoebisch, E. G.; Healy, E. F., Stewart, J. J. P. Development and use of quantum mechanical molecular models. 76. AM1: a new general purpose quantum mechanical molecular model, **J. Am. Chem. Soc.**, v. 107, n. 13, 1985, p. 3902-3909.

[33] Stewart, J. J. P. Optimization of parameters for semiempirical methods I. Method, **J. Comput. Chem.**, v. 10, n. 2, 1989, p. 209-220.

[34] Stewart, J. J. P. Optimization of parameters for semiempirical methods II. Applications, **J. Comput. Chem.**, v. 10, n. 2, 1989, p. 221-264.

[35] Machado, P.; Campos, P. T.; Lima, G. R.; Rosa, F. A.; Flores, A. F. C.; Bonacorso, H. G.; Zanatta, N.; Martins, M. A. P. Experimental and calculated structural parameters of 5-trihalomethyl-4,5-dihydro-1*H*-pyrazole derivatives, novel analgesic agents, **J. Mol. Struct.**, v. 917, n. 2-3, 2009, p. 176-182.

[36] Quémard, A.; Sacchettini, J. C.; Dessen, A.; Vilchèze, C.; Bittman, R.; Jacobs, W. R. Jr.; Blanchard, J. S. Enzymatic characterization of the target for isoniazid in *Mycobacterium tuberculosis*, **Biochemistry**, v. 34, n. 26, 1995, p. 8235-8241.

[37] Basso, L. A.; Zheng, R.; Musser, J. M.; Jacobs, W. R. Jr.; Blanchard, J. S. Mechanisms of isoniazid resistance in *Mycobacterium tuberculosis*: enzymatic characterization of enoyl reductase mutants identified in isoniazid-resistant clinical isolates, **J. Infect. Dis.**, v. 178, n. 3, 1998, p. 769-775.

[38] Laurence, C.; Brameld, K. A.; Graton, J.; Le Questel, J. Y.; Renault, E. The pK_{BHX} database: toward a better understanding of hydrogen-bond basicity for medicinal chemists, **J. Med. Chem.**, v. 52, n. 14, 2009, p. 4073-4086.

[39] Matviiuk, T.; Rodriguez, F.; Saffon, N.; Mallet-Ladeira, S.; Gorichko, M.; de Jesus, A. L. L. R.; Pasca, M. R.; Lherbet, C.; Voitenko, Z.; Baltas, M. Design, chemical synthesis of 3-(9*H*-fluoren-9-yl)pyrrolidine-2,5-dione derivatives and biological activity against enoyl-ACP reductase (InhA) and *Mycobacterium tuberculosis,* **Eur. J. Med. Chem.***;* v. 70, 2013, p. 37-48.

[40] Matviiuk, T.; Mori, G.; Lherbet, C.; Rodriguez, F.; Pasca, M. R.; Gorichko, M.; Guidetti, B.; Voitenko, Z.; Baltas, M. Synthesis of 3-heteryl substituted pyrrolidine-2,5-diones via catalytic Michael reaction and evaluation of their inhibitory activity against InhA and *Mycobacterium tuberculosis,* **Eur. J. Med. Chem.**, v. 71, 2014, p. 46-52.

[41] Punkvang, A.; Saparpakorn, P.; Hannongbua, S.; Wolschann, P.; Berner, H.; Pungpo, P. Insight into crucial inhibitor-enzyme interaction of arylamides as novel direct inhibitors of the enoyl ACP reductase (InhA) from *Mycobacterium tuberculosis*: computer-aided molecular design, **Monatsh. Chem**., v. 141, n. 9, 2010, p. 1029-1041.

[42] Clark, D. T.; Murrell, J. N.; Tedder, J. M. 234. The magnitudes and signs of the inductive and mesomeric effects of the halogens, **J. Chem. Soc.**, 1963, p. 1250-1253.

[43] Bissantz, C.; Kuhn, B.; Stahl, M. A medicinal chemist's guide to molecular interactions, **J. Med. Chem.**, v. 53, 2010, p. 5061–5084.

[44] Cleland, W. W.; Cook, P. F. Enzyme Kinetics and Mechanism, Garland Science Publishing, New York, 2007, ch. 6, pp. 121-204.

[45] Copeland, R. A. Evaluation of Enzyme Inhibitors in Drug Discovery: A Guide for Medicinal Chemists and Pharmacologists, 1st ed.; John Wiley & Sons: Hoboken, NJ, 2005; Chapter 3 and 5.

[46] Sheldrick, G. M. SHELXS-97: Program for Crystal Structure Solution, University of Göttingen, Germany, 1997.

[47] Sheldrick, G. M. SHELXL-97: Program for Crystal Structure Refinement, University of Göttingen, Germany, 1997.

[48] Farrugia, L. J. ORTEP-3 for windows - a version of ORTEP-III with a graphical user interface (GUI), **J. Appl. Cryst.**, v. 30, n. 5, 1997, p. 565.

[49] Kumar, C. S. A.; Prasad, S. B. B.; Thimmegowda, N. R.; Rangappa, K. S.; Chandrappa, S.; Naveen, S.; Sridhar, M. A.; Prasad, J. S. Synthesis and crystal structure of 1-benzenesulfonyl-4-benzhydrylpiperazine, **Mol. Cryst. Liq. Cryst.**, v. 469, n. 1, 2007, p.111-119.

[50] HYPERCHEM$^{(TM)}$ Professional 7.52 (2002), Hypercube, Inc., 1115 NW 4th Street, Gainesville, FL 32601, USA.

[51] Morris, G. M.; Huey, R.; Lindstrom, W.; Sanner, M. F.; Belew, R. K.; Goodsell, D. S.; Olson, A. J. (2009) Autodock4 and AutoDockTools4: automated docking with selective receptor flexibility, **J. Comput. Chem.** v. 16, 2009, p. 2785-2791.

[52] Morris, G. M.; Goodsell, D. S.; Halliday, R.S.; Huey, R.; Hart, W. E.; Belew, R. K.; Olson, A. J. Automated Docking Using a Lamarckian Genetic Algorithm and Empirical Binding Free Energy Function, J**. Comput. Chem**., v. 19, 1998, p. 1639-1662.

[53] Parikh, S.; Moynihan, D. P.; Xiao, G.; Tonge, P. T. Roles of tyrosine 158 and lysine 165 in the catalytic mechanism of InhA, the enoyl-ACP reductase from *Mycobacterium tuberculosis*, **Biochemistry**, 1999, v. 38, n. 41, p. 13623-13634.

[54] Bradford, M. M. A rapid and sensitive method for the quantification of microgram quantities of protein utilizing the principle os protein-dye binding. **Anal. Biochem.**, v. 72, 1976, p. 248-254.

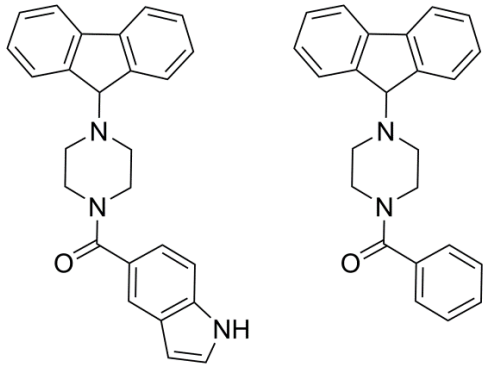

1 (Genz-10850) **2**

Figure 1. Chemical structures of piperazine derivatives identified as potent *Mt*InhA inhibitors through HTS.

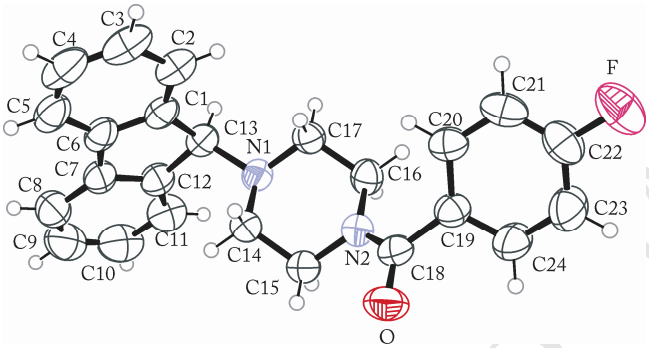

Figure 2. A view of compound **4d** with atomic labeling. Hydrogen atoms are represented by circles of arbitrary radii.

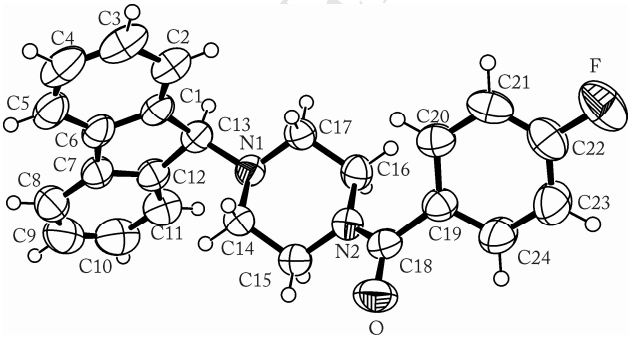

Figure 2. A view of compound **4d** with atomic labeling. Hydrogen atoms are represented by circles of arbitrary radii.

(A color figure is available in the web version of the manuscript).

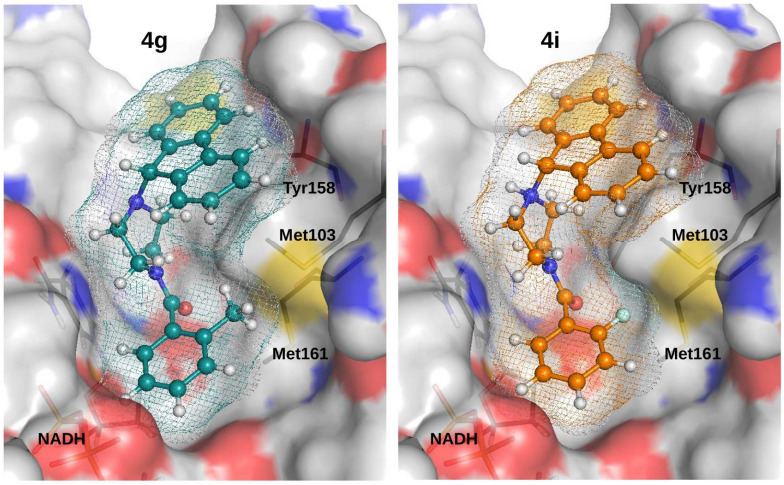

Figure 3. Best binding modes of inhibitor compounds **4g** and **4i** (represented by ball and stick models embedded in their meshed molecular surface) to the binary complex *Mt*InhA-NADH (represented as a solid molecular surface colored by CPK) from docking simulations. Closer inspection of the docked complexes suggests a steric hindrance produced by the methyl group which is observed to a minor extent for a fluorine atom.

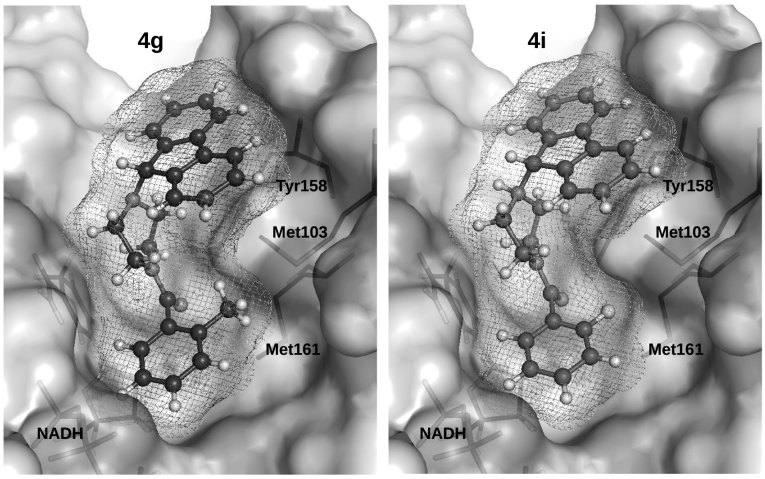

Figure 3. Best binding modes of inhibitor compounds **4g** and **4i** (represented by ball and stick models embedded in their meshed molecular surface) to the binary complex *Mt*InhA-NADH (represented as a solid molecular surface colored by CPK) from docking simulations. Closer inspection of the docked complexes suggests a steric

hindrance produced by the methyl group which is observed to a minor extent for a fluorine atom.

(A color figure is available in the web version of the manuscript).

Table 1. Determined IC_{50} values of piperazine derivatives for the *Mt*InhA-catalyzed reaction.

Comp.	IC_{50} (µM)[a]	*Comp.*	IC_{50} (µM)[a]
2	0.183 (± 0.005)	**5b**	> 50
4a	2.90 (± 0.45)	**6**	> 50
4b	0.222 (± 0.03)	**7**	> 50
4c	1.69 (± 0.56)	**8**	> 50
4d	0.397 (± 0.04)	**10a**	16.03 (± 2.86)
4e	> 50	**10b**	> 50
4f	0.250 (± 0.02)	**10c**	7.83 (± 1.27)
4g	5.99 (± 0.94)	**10d**	> 50
4h	0.240 (± 0.04)	**10e**	> 50
4i	0.361 (± 0.04)	**10f**	> 50
4j	1.57 (± 0.17)	**11**	> 50
4k	9.77 (± 1.30)	**12**	> 50
5a	19.96 (± 2.45)		

[a]IC_{50} is the concentration of inhibitor that reduces the enzyme velocity by half under a specific set of reaction conditions.

Table 2. Inhibition constants of select compounds on *Mt*InhA activity.

Comp.	*NADH*	*Inhibition mode*	*DD-CoA*		*Inhibition mode*
	K_{ii} (µM)[a]		K_{is} (µM)[b]	K_{ii} (µM)	
2	0.155 (± 0.01)	Uncompetitive	0.100 (± 0.03)	0.425 (± 0.18)	Noncompetitive
4a	1.95 (± 0.16)	Uncompetitive	1.60 (± 0.53)	7.22 (± 6.77)	Noncompetitive
4b	0.181 (± 0.01)	Uncompetitive	0.101 (± 0.02)	-	Competitive
4c	1.12 (± 0.04)	Uncompetitive	2.77 (± 2.08)	2.00 (± 4.62)	Noncompetitive
4d	0.348 (± 0.06)	Uncompetitive	0.338 (± 0.10)	-	Competitive
4f	0.185 (± 0.01)	Uncompetitive	0.162 (± 0.03)	0.348 (± 0.14)	Noncompetitive
4h	0.147 (± 0.004)	Uncompetitive	0.118 (± 0.02)	-	Competitive
4i	0.332 (± 0.04)	Uncompetitive	0.149 (± 0.06)	0.660 (± 0.60)	Noncompetitive
4j	1.28 (± 0.09)	Uncompetitive	0.788 (± 0.26)	3.25 (± 1.56)	Noncompetitive

[a]K_{ii} is the inhibitory dissociation constant for the ESI complex; [b]K_{is} is the inhibitory dissociation constant for the EI complex [44].

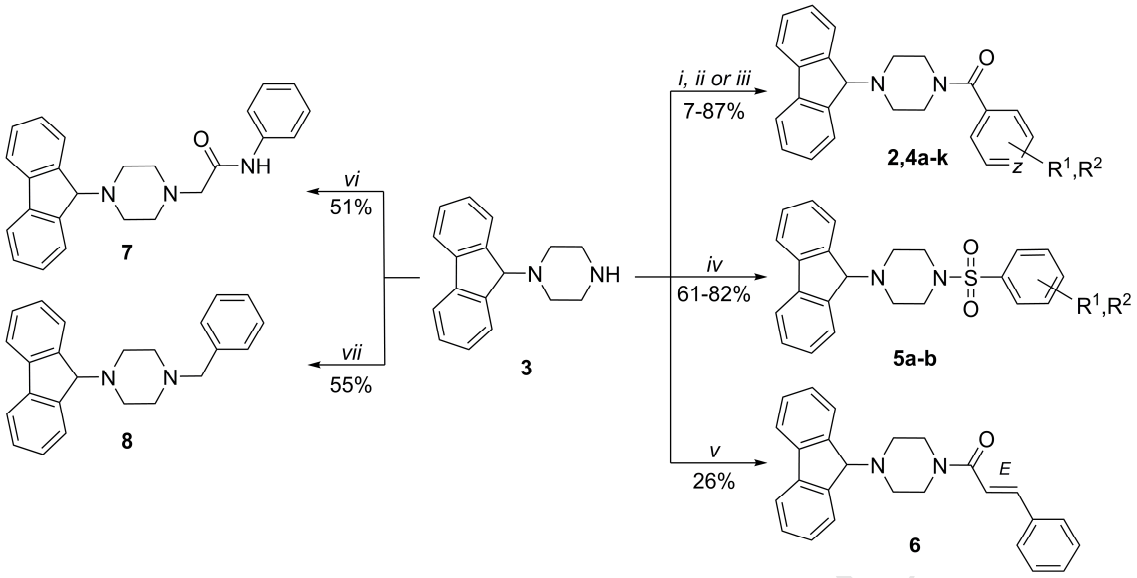

Comp.	R^1	R^2	*z*	*Yield (%)*
2	H	H	C	42
4a	4-OMe	H	C	87
4b	4-Me	H	C	55
4c	4-Cl	H	C	7
4d	4-F	H	C	8
4e	4-NO_2	H	C	24
4f	3-Me	H	C	77
4g	2-Me	H	C	83
4h	3-F	H	C	8
4i	2-F	H	C	32
4j	2-F	5-F	C	87
4k	H	H	N	83
5a	H	H	-	61
5b	2-Me	H	-	82

Scheme 1. Reactants and conditions: *i)* = (1) Benzoic acid, $SOCl_2$, toluene, 110 °C, 5 h; (2) TEA, CH_2Cl_2, 0-25 °C, 16 h. *ii)* = Benzoyl chloride, TEA, CH_2Cl_2, 0-25 °C, 16 h. *iii)* = Benzoic acid, HBTU, TEA, 25 °C, 4 h. *iv)* = Benzenesulfonyl chloride, TEA, CH_2Cl_2, 0-25 °C, 16 h. *v)* = (1) Cinnamic acid, $SOCl_2$, toluene, 110 °C, 5 h; (2) TEA, CH_2Cl_2, 0-25 °C, 16 h. *vi)* = 2-Bromo-*N*-phenylacetamide, K_2CO_3, DMF, 25 °C, 24 h. *vii)* = (Bromomethyl)benzene, K_2CO_3, DMF, 25 °C, 24 h.

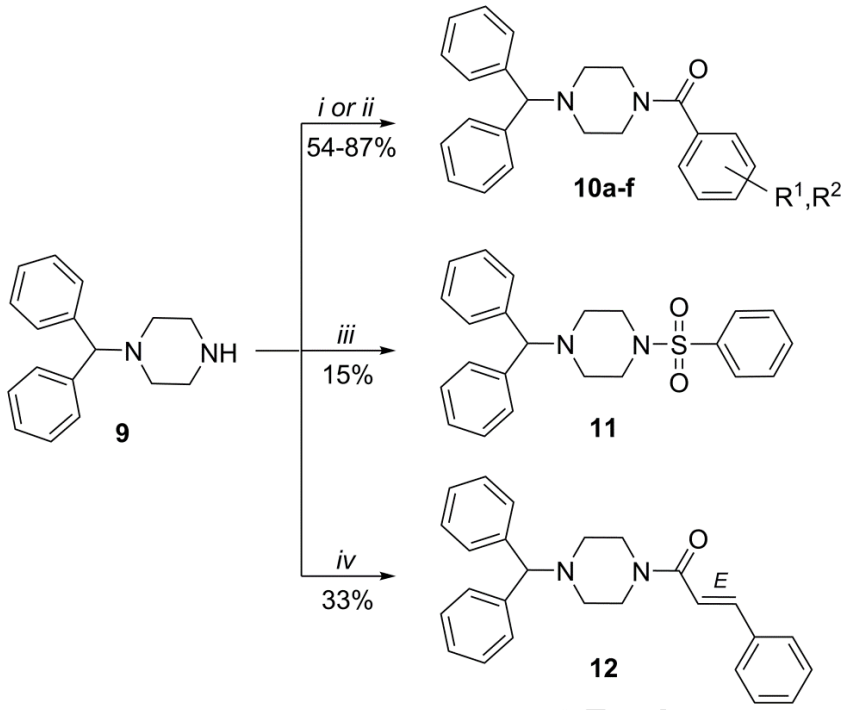

Comp.	R^1	R^2	*Yield (%)*
10a	H	H	87
10b	4-OMe	H	37
10c	4-Me	H	55
10d	4-Cl	H	60
10e	4-F	H	54
10f	2-F	5-F	82

Scheme 2. Reactants and conditions: *i)* = (1) Benzoic acid, $SOCl_2$, toluene, 110 °C, 5 h; (2) TEA, CH_2Cl_2, 0-25 °C, 16 h. *ii)* = Benzoyl chloride, TEA, CH_2Cl_2, 0-25 °C, 16 h. *iii)* = Benzenesulfonyl chloride, TEA, CH_2Cl_2, 0-25 °C, 16 h. *iv)* = (1) Cinnamic acid, $SOCl_2$, toluene, 110 °C, 5 h; (2) TEA, CH_2Cl_2, 0-25 °C, 16 h.

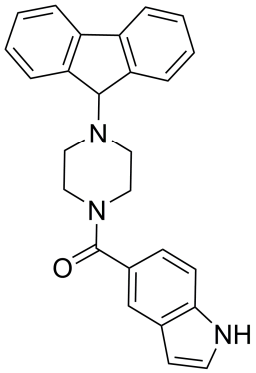

1 (Genz-10850)

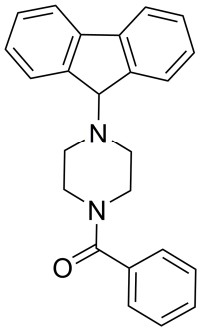

2

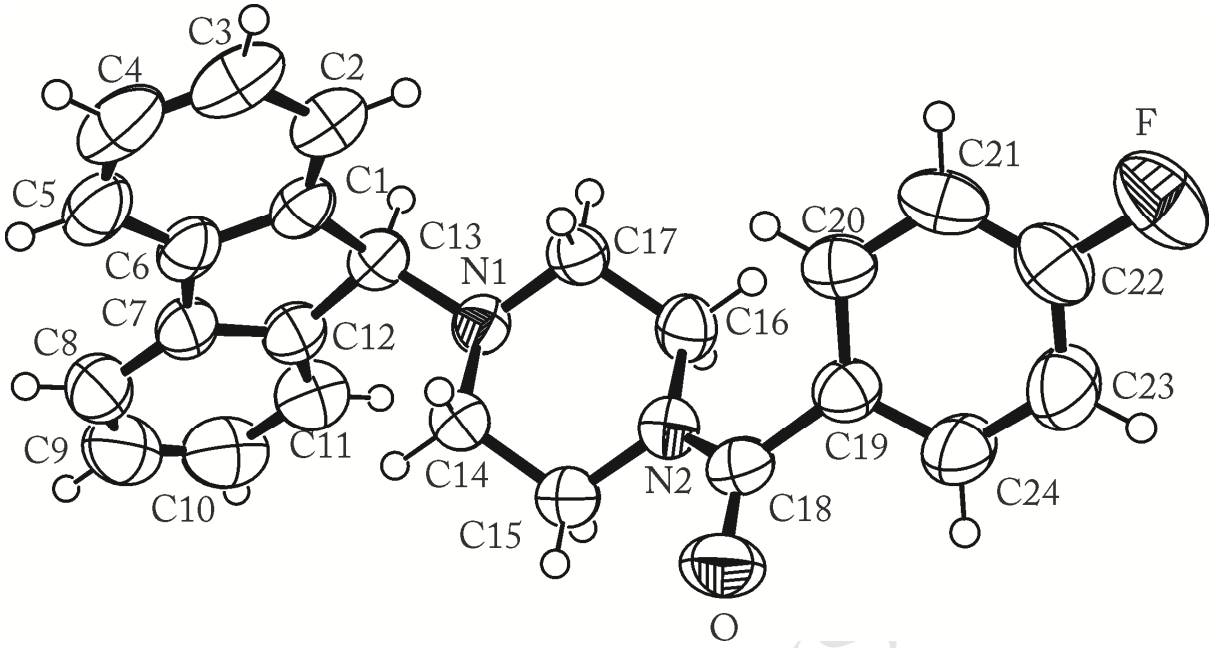

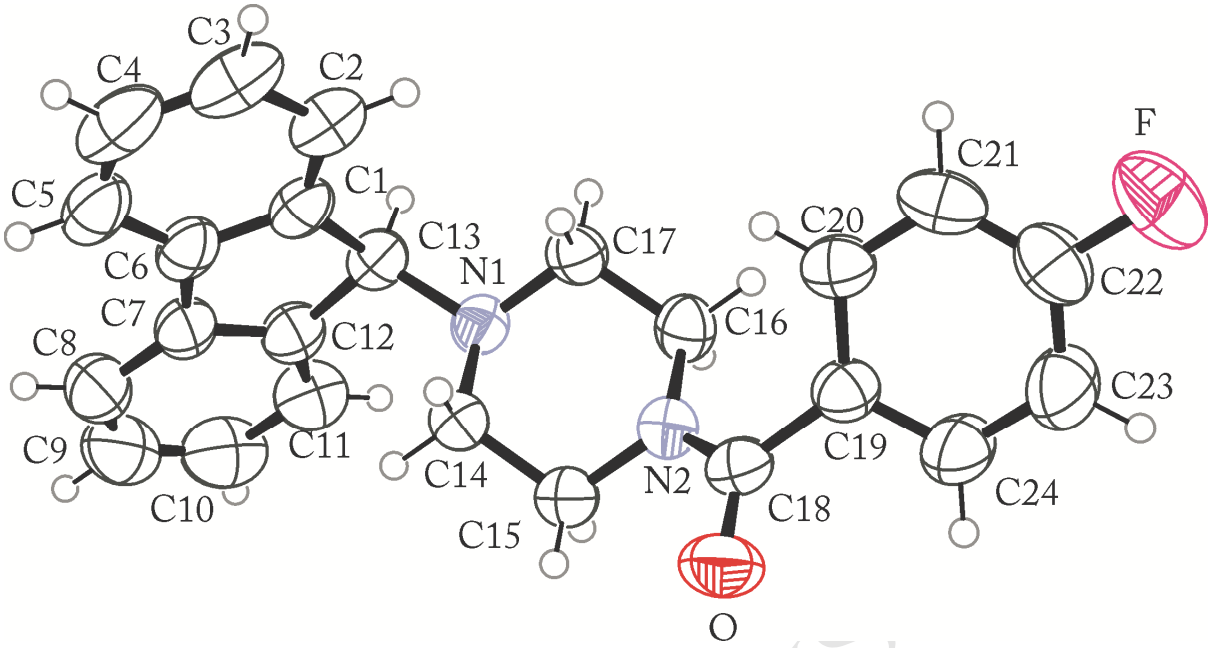

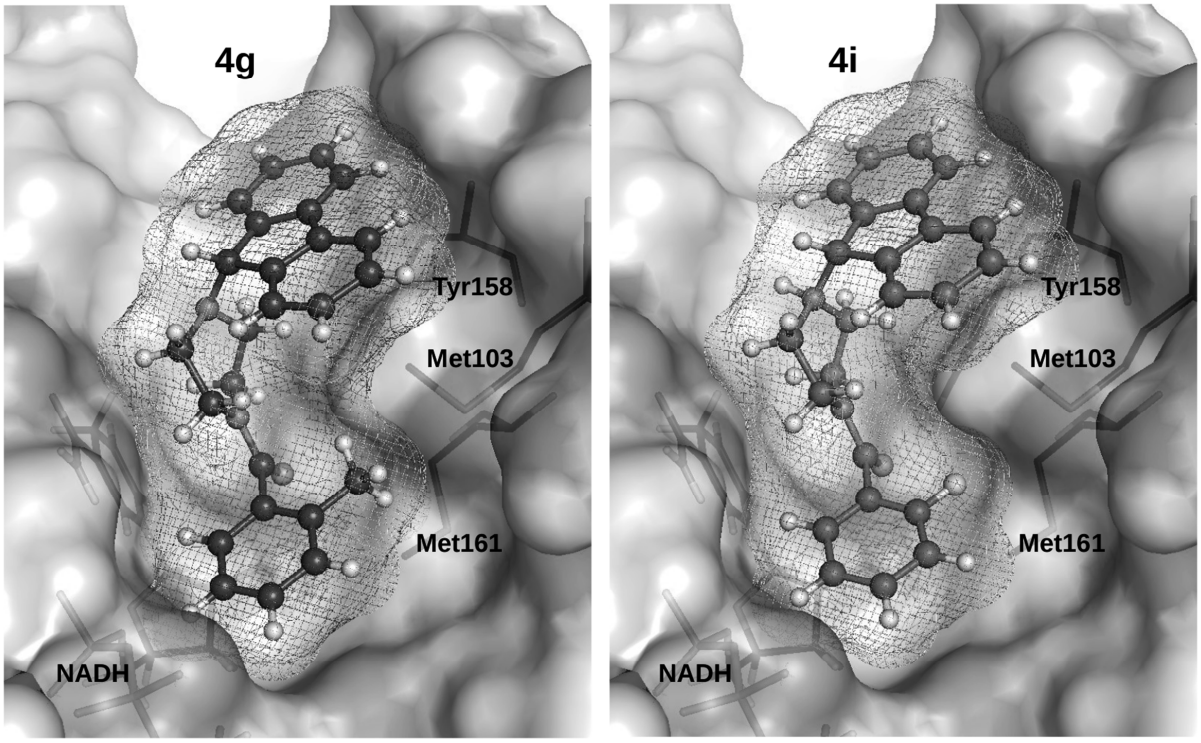

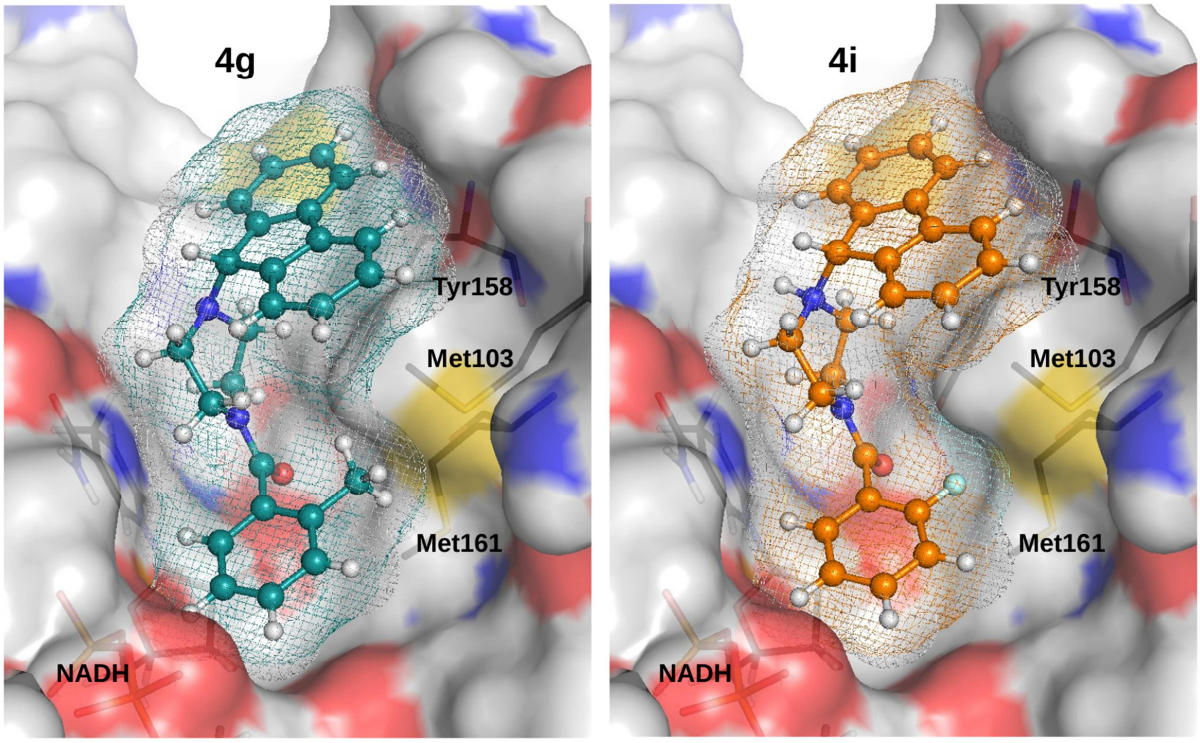

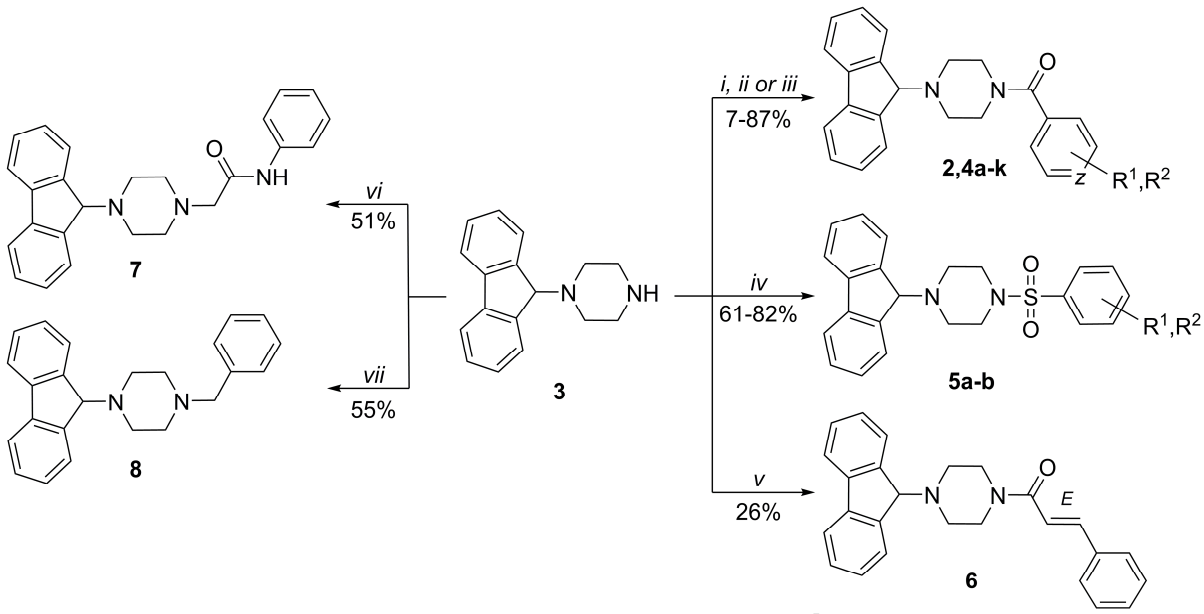

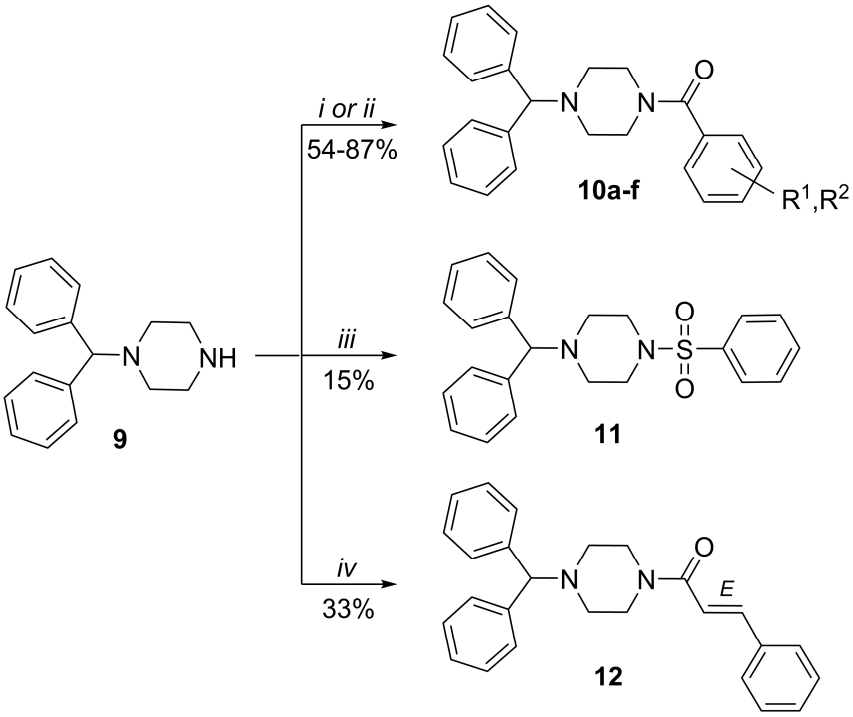

Highlights:

Synthesis and structural characterization of piperazine derivatives.

Identification of *Mt*InhA inhibitors with IC_{50} values and inhibition constants in the submicromolar range.

Electronic and structural characterization of the pharmacophore carbonyl group environment of the compounds.

In vitro kinetic assays to characterize the binding mode of the inhibitors.

MIC determination to evaluate the inhibitory capacity of select compounds.

Supporting Information

Piperazine derivatives: synthesis, inhibition of the *Mycobacterium tuberculosis* enoyl-acyl carrier protein reductase and SAR studies

Mariane Rotta, Kenia Pissinate, Anne Drumond Villela, Davi Fernando Back, Luis Fernando Saraiva Macedo Timmers, José Fernando Ruggiero Bachega, Osmar Norberto de Souza, Diógenes Santiago Santos*, Luiz Augusto Basso, Pablo Machado*

TABLE OF CONTENTS

1. ^{1}H NMR spectra of compounds 2 and 4j

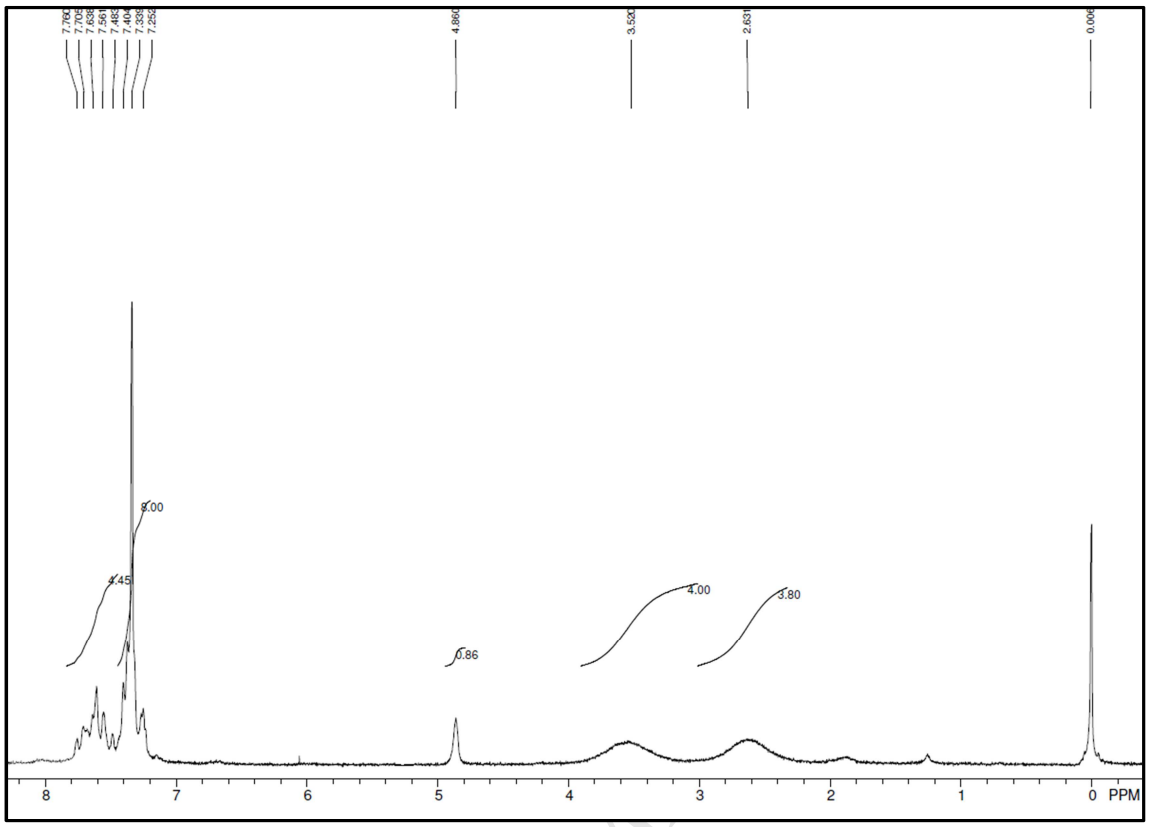

Figure S1. ^{1}H NMR spectra of compound **2**.

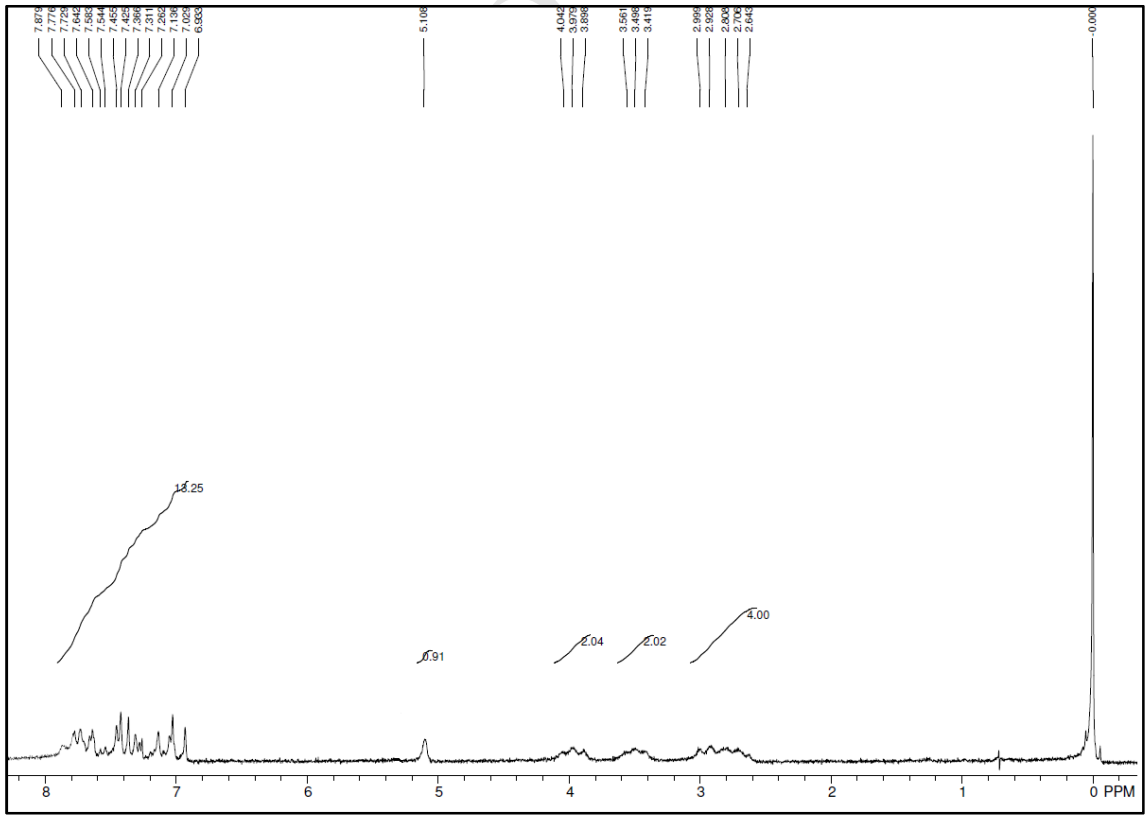

Figure S2. ^{1}H NMR spectra of compound **4j**.

*2. ^{13}C NMR spectra of compounds **2** and **4j***

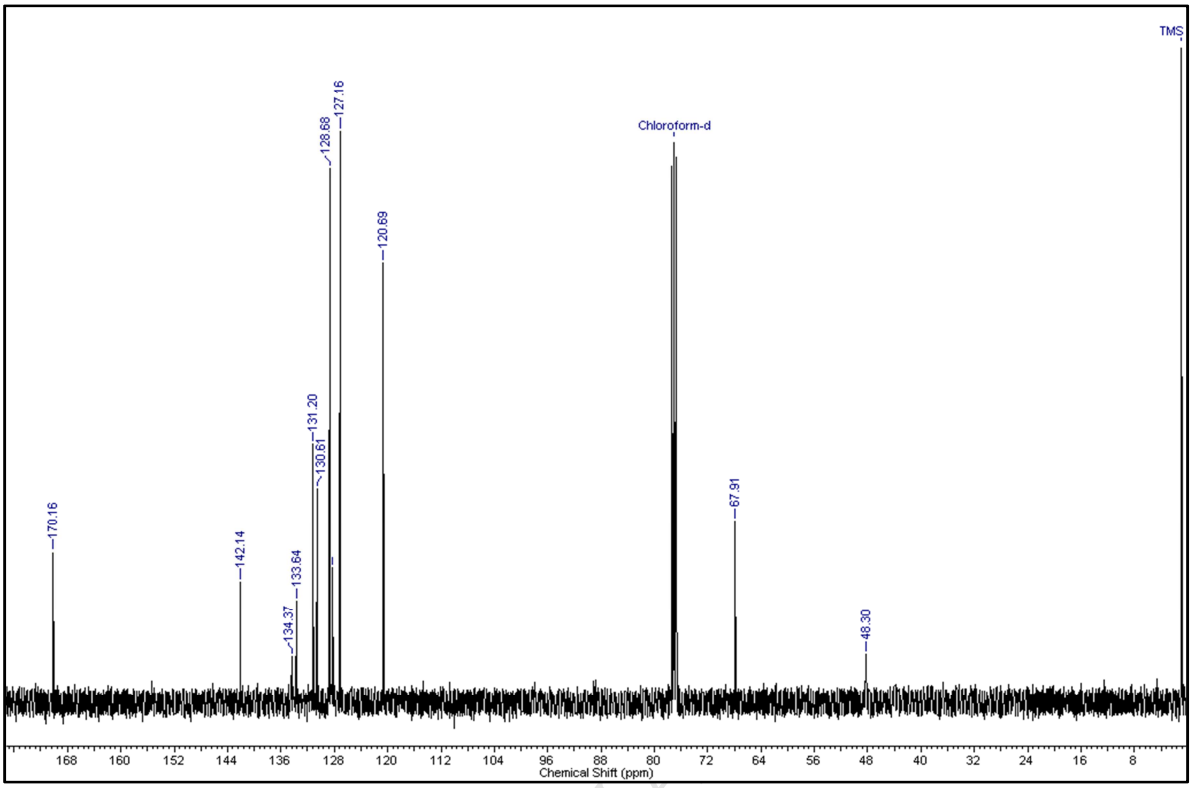

Figure S3. ^{13}C NMR spectra of compound **2**.

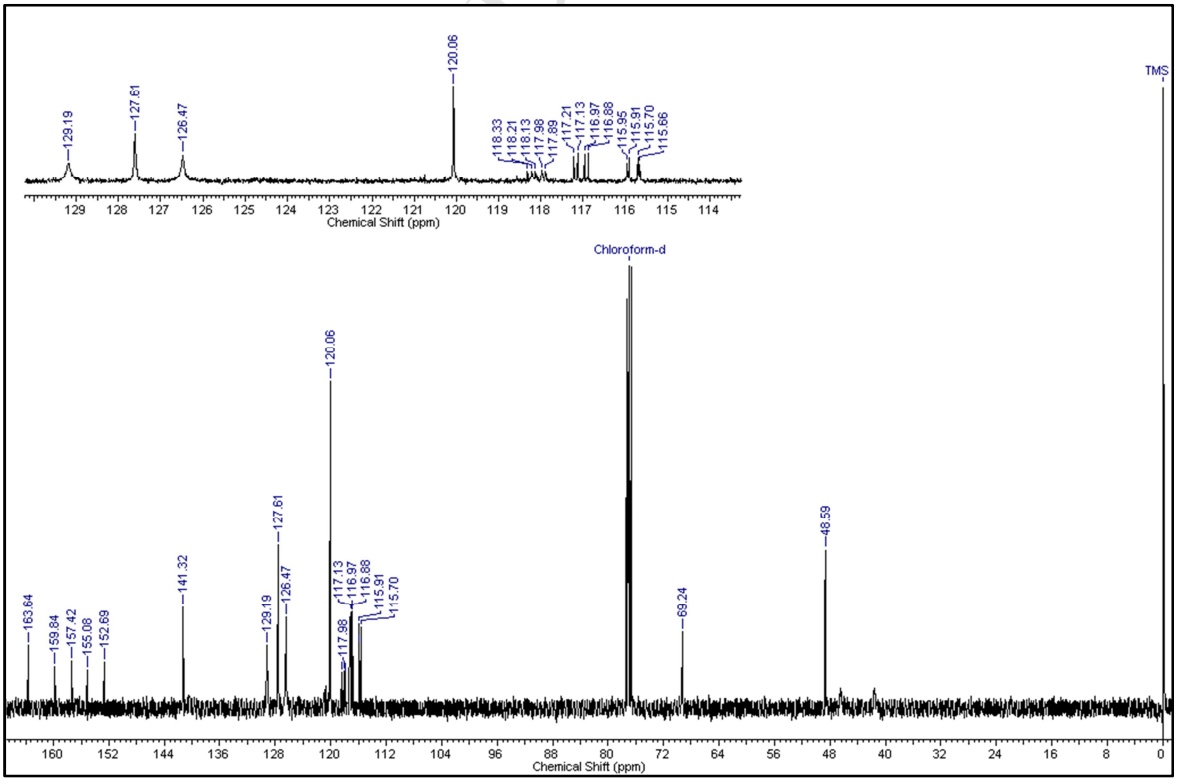

Figure S4. ^{13}C NMR spectra of compound **4j**.

3. *Lineweaver-Burk plots of compounds* ***2***, ***4a***, ***4b, 4c***, ***4d***, ***4f***, ***4h***, ***4i***, *and* ***4j***

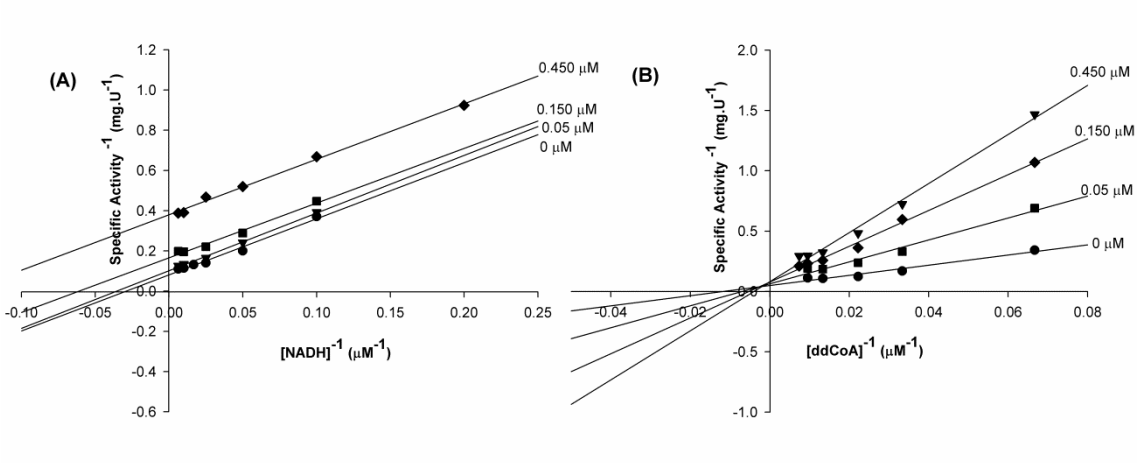

Figure S5. Double-reciprocal plots of inhibition assays for compound **2**. Pattern of parallel lines indicate uncompetitive inhibition towards NADH **(A)**, whereas pattern of intersection at left of *y*-axis indicate noncompetitive inhibition towards DD-CoA **(B)**.

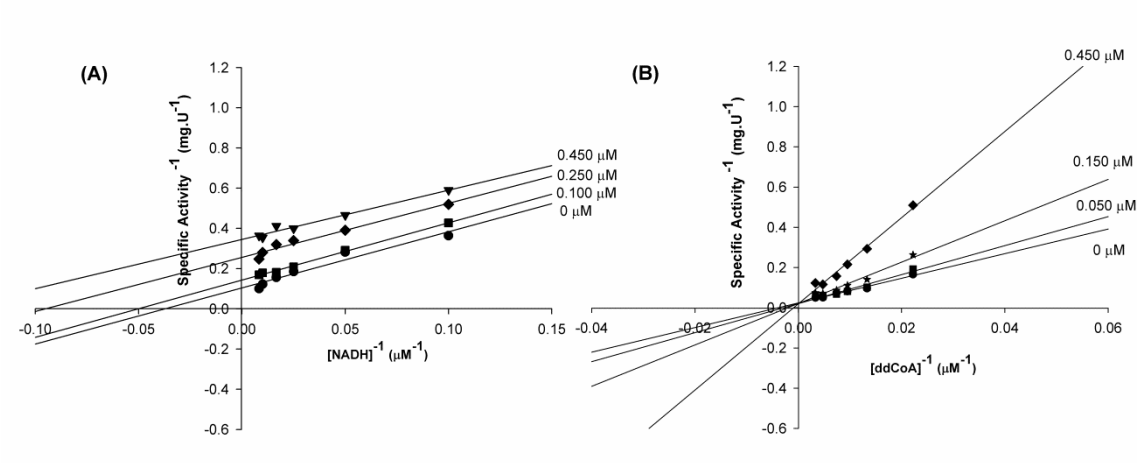

Figure S6. Double-reciprocal plots of inhibition assays for compound **2** with saturating concentration of DD-CoA substrate (**A**) and with saturating concentration of NADH substrate (**B**). Pattern of parallel lines indicate uncompetitive inhibition towards NADH (**A**), whereas patter of intersection lines at *y*-axis indicate competitive inhibition towards DD-CoA **(B)**.

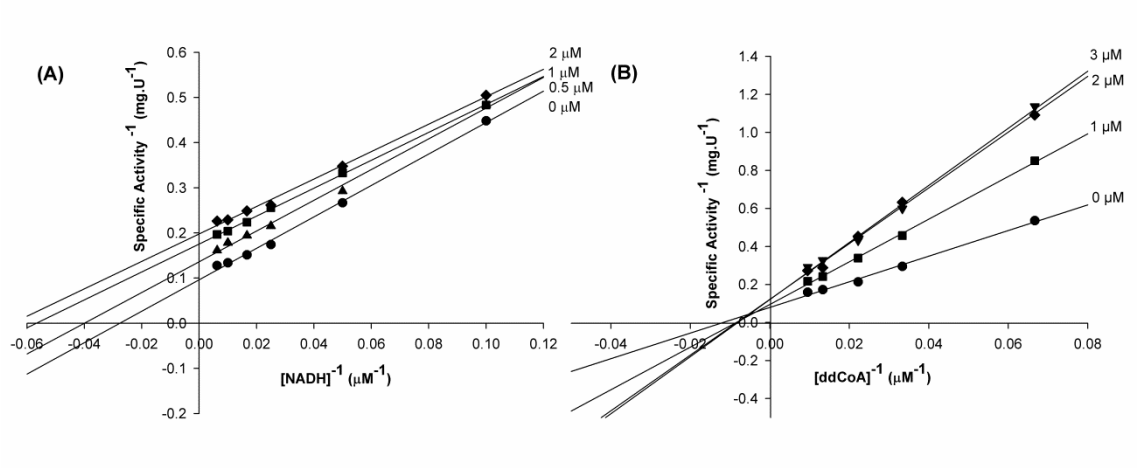

Figure S7. Double-reciprocal plots of inhibition assays for compound **4a**. Pattern of parallel lines indicate uncompetitive inhibition towards NADH **(A)**, whereas pattern of intersection at left of *y*-axis indicate noncompetitive inhibition towards DD-CoA **(B)**.

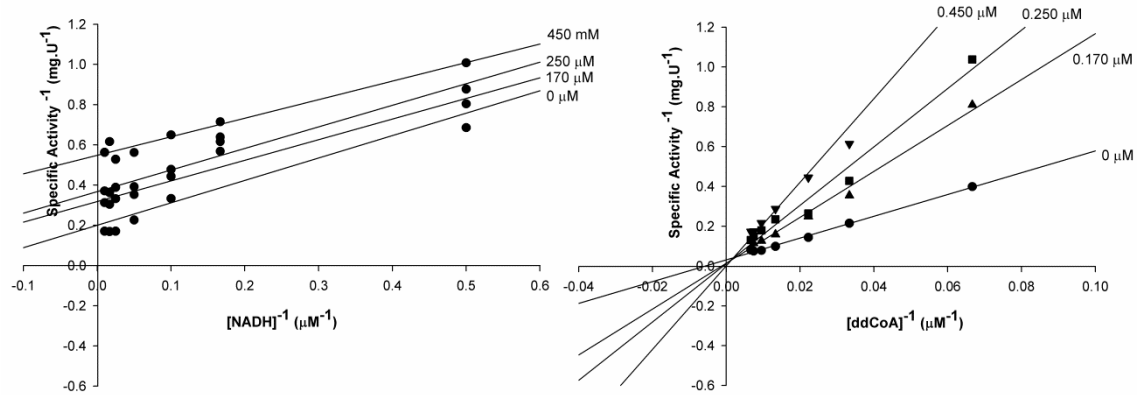

Figure S8. Double-reciprocal plots of inhibition assays for compound **4b**. Pattern of parallel lines indicate uncompetitive inhibition towards NADH **(A)**, whereas pattern of intersection at *y*-axis indicate competitive inhibition towards DD-CoA **(B)**.

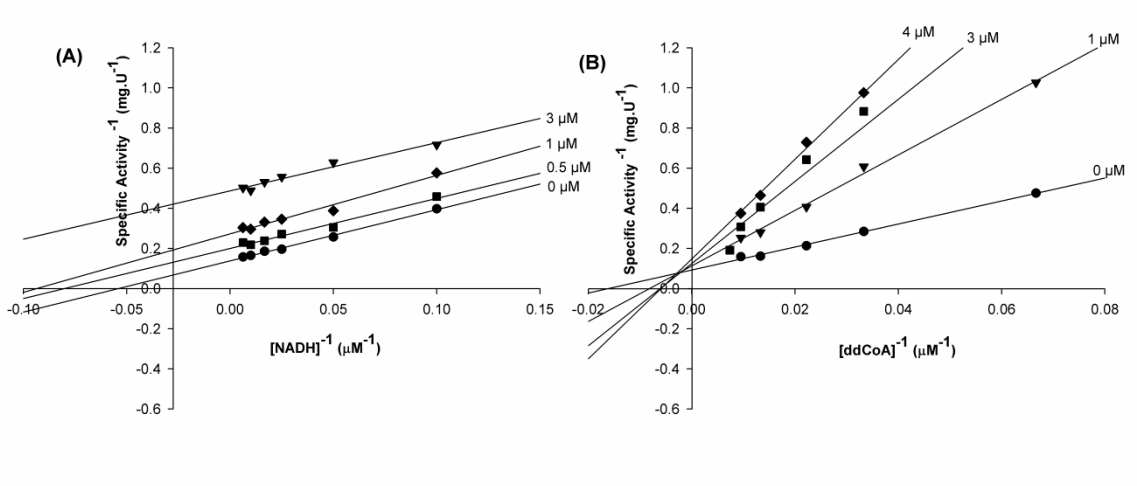

Figure S9. Double-reciprocal plots of inhibition assays for compound **4c**. Pattern of parallel lines indicate uncompetitive inhibition towards NADH (**A**), whereas pattern of intersection at left of *y*-axis indicate noncompetitive inhibition towards DD-CoA (**B**).

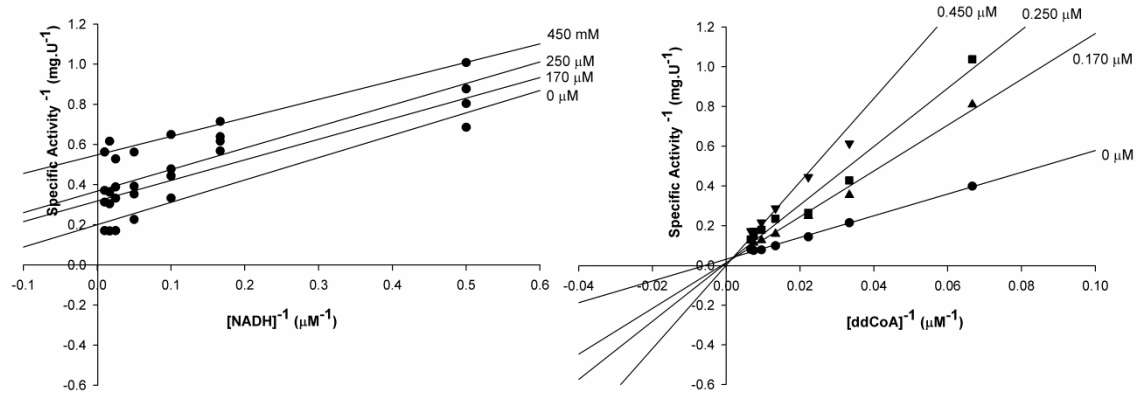

Figure S10. Double-reciprocal plots of inhibition assays for compound **4d**. Pattern of parallel lines indicate uncompetitive inhibition towards NADH (**A**), whereas pattern of intersection at left of *y*-axis indicate noncompetitive inhibition towards DD-CoA (**B**).

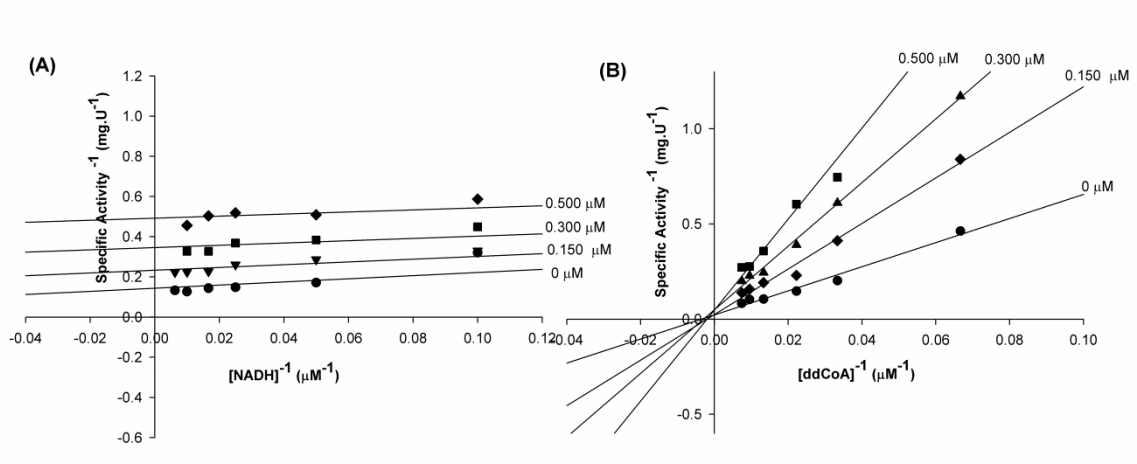

Figure S11. Double-reciprocal plots of inhibition assays for compound **4f**. Pattern of parallel lines indicate uncompetitive inhibition towards NADH **(A)**, whereas pattern of intersection at left of *y*-axis indicate noncompetitive inhibition towards DD-CoA **(B)**.

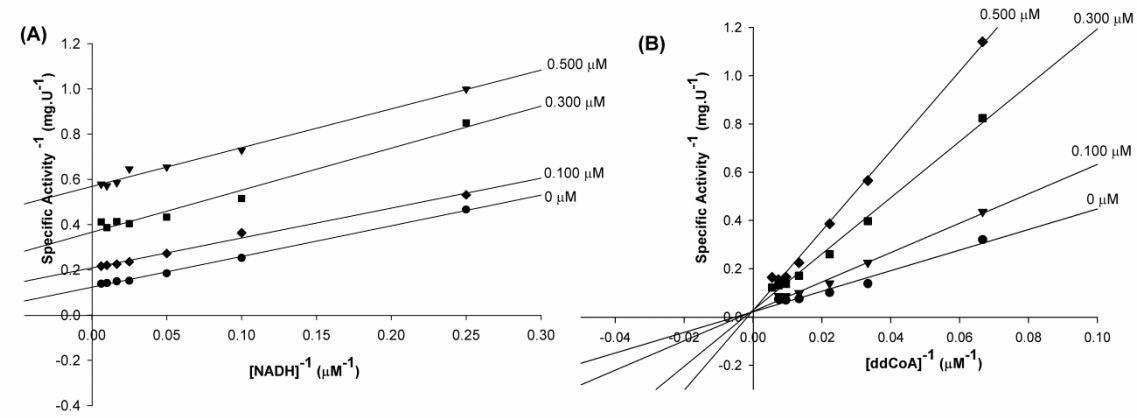

Figure S12. Double-reciprocal plots of inhibition assays for compound **4h**. Pattern of parallel lines indicate uncompetitive inhibition towards NADH (**A**), whereas pattern of intersection at *y*-axis indicate competitive inhibition towards DD-CoA (**B**).

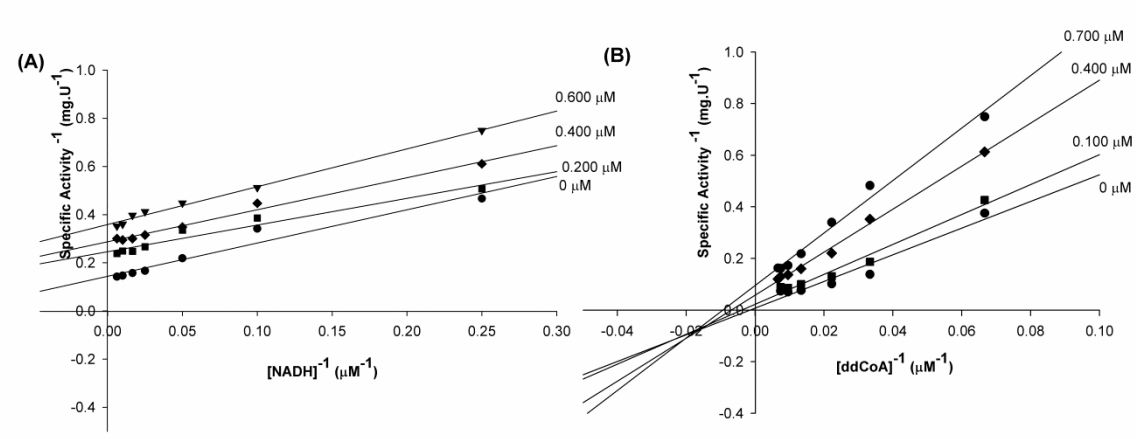

Figure S13. Double-reciprocal plots of inhibition assays for compound **4i**. Pattern of parallel lines indicate uncompetitive inhibition towards NADH (**A**), whereas pattern of intersection at left of *y*-axis indicate noncompetitive inhibition towards DD-CoA (**B**).

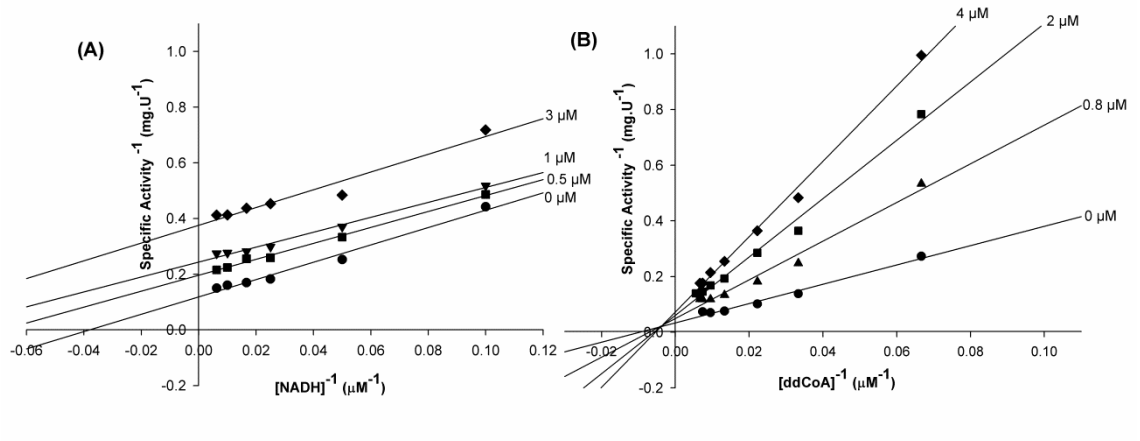

Figure S14. Double-reciprocal plots of inhibition assays for compound **4j**. Pattern of parallel lines indicate uncompetitive inhibition towards NADH (**A**), whereas pattern of intersection at left of *y*-axis indicate noncompetitive inhibition towards DD-CoA (**B**).

Table S1. Crystal data and structure refinement for **4d**.

Parameters	
CCDC N°	1000538
Formula	$C_{24}H_{21}FN_2O$
M_r	372.43
Temperature (K)	100 (2)
Wavelength (Å)	0.71073
Crystal system	Monoclinic
Space group	$P2_1/n$
Unit cell parameters	
a (Å)	10.1824 (2)
b (Å)	20.2972 (5)
c (Å)	10.2704 (2)
β (°)	117.458 (10)
V (Å^3)	1883.51 (7)
Z	4
Density (calculated) (g·cm^{-3})	1.313
Absorption coefficient (mm^{-1})	0.088
*T*min/*T*max	0.9493/0.9650
F (000)	784
Crystal size (mm)	0.60 × 0.55 × 0.41
θ range for data collection (°)	2.01 to 27.15
h, k, l range	-12 ≤ h ≤ 13 -26 ≤ k ≤ 24 -12 ≤ l ≤ 13
Reflections collected	29997
Independent reflections	4076 [R(int) = 0.0230]
Data/restraints/parameters	4076/0/254
Absorption correction	Gaussian
Refinement method	Full-matrix least-squares on F^2
Final R indices [I > 2σ(I)]	R1 = 0.0395, wR2 = 0.0997
R indices (all data)	R1 = 0.0628, wR2 = 0.1115
Goodness of fit on F^2	1.033
Extinction coefficient	0.0096 (12)
Largest diff. peak and hole (e Å^{-3})	0.147 and -0.164

Table S2. Selected bond lengths (Å) obtained experimentally and calculated with PM3 and AM1 method for **4d**.

Bond length	X-ray	PM3	AM1
F-C(22)	1.358	1.342	1.353
O-C(18)	1.227	1.220	1.247
N(1)-C(14)	1.455	1.494	1.447
N(1)-C(17)	1.460	1.489	1.447
N(1)-C(13)	1.469	1.489	1.448
C(13)-C(12)	1.518	1.516	1.529
C(13)-C(1)	1.530	1.516	1.529
C(22)-C(23)	1.348	1.400	1.407
C(22)-C(21)	1.361	1.400	1.407
C(21)-C(20)	1.386	1.388	1.391
C(20)-C(19)	1.381	1.396	1.398
C(19)-C(24)	1.386	1.396	1.399
C(19)-C(18)	1.496	1.495	1.491
C(18)-N(2)	1.348	1.438	1.394
N(2)-C(15)	1.458	1.488	1.448
N(2)-C(16)	1.459	1.487	1.445
C(15)-C(14)	1.515	1.528	1.544
C(12)-C(11)	1.376	1.382	1.381
C(12)-C(7)	1.395	1.413	1.423
C(7)-C(8)	1.386	1.384	1.385
C(7)-C(6)	1.463	1.461	1.459
C(8)-C(9)	1.372	1.396	1.401
C(9)-C(10)	1.372	1.390	1.391
C(23)-C(24)	1.371	1.389	1.390
C(16)-C(17)	1.513	1.528	1.546
C(11)-C(10)	1.391	1.397	1.403
C(6)-C(5)	1.391	1.384	1.385
C(6)-C(1)	1.396	1.414	1.426
C(1)-C(2)	1.382	1.381	1.381
C(2)-C(3)	1.392	1.390	1.403
C(3)-C(4)	1.378	1.396	1.391
C(4)-C(5)	1.370	1.396	1.401

Table S3. Selected bond angles (°) obtained experimentally and calculated with PM3 and AM1 method for **4d**.

Bond angle	X-ray	PM3	AM1
C(14)-N(1)-C(17)	109.94	113.06	113.80
C(14)-N(1)-C(13)	113.44	112.17	117.27
C(17)-N(1)-C(13)	114.64	113.69	116.52
N(1)-C(13)-C(12)	111.55	116.39	111.93
N(1)-C(13)-C(1)	118.80	112.72	119.45
C(12)-C(13)-C(1)	101.46	102.17	101.83
C(23)-C(22)-F	118.43	119.40	119.84
C(23)-C(22)-C(21)	122.79	121.28	120.35
F-C(22)-C(21)	118.78	119.32	119.80
C(22)-C(21)-C(20)	118.46	118.89	119.45
C(19)-C(20)-C(21)	120.59	120.24	120.29
C(20)-C(19)-C(24)	118.20	120.47	120.13
C(20)-C(19)-C(18)	124.20	119.97	121.25
C(24)-C(19)-C(18)	117.33	119.48	118.51
O-C(18)-N(2)	121.27	118.90	120.60
O-C(18)-C(19)	118.87	121.73	120.21
N(2)-C(18)-C(19)	119.86	119.22	119.08
C(18)-N(2)-C(15)	119.86	118.38	119.29
C(18)-N(2)-C(16)	128.04	118.66	122.18
C(15)-N(2)-C(16)	111.87	110.59	114.02
N(2)-C(15)-C(14)	109.69	112.44	114.40
N(1)-C(14)-C(15)	109.83	111.34	117.09
C(11)-C(12)-C(7)	120.48	120.53	120.71
C(11)-C(12)-C(13)	128.69	129.27	128.81
C(7)-C(12)-C(13)	110.83	110.30	110.45
C(8)-C(7)-C(12)	120.33	120.93	120.75
C(8)-C(7)-C(6)	131.07	130.45	130.93
C(12)-C(7)-C(6)	108.58	108.60	108.62
C(9)-C(8)-C(7)	118.71	118.28	118.68
C(8)-C(9)-C(10)	121.26	120.93	120.87
C(22)-C(23)-C(24)	118.57	119.01	119.43
C(23)-C(24)-C(19)	121.38	120.10	120.31
N(2)-C(16)-C(17)	109.28	111.82	113.47
N(1)-C(17)-C(16)	109.81	110.79	115.53
C(12)-C(11)-C(10)	118.63	118.58	118.52
C(9)-C(10)-C(11)	120.59	120.88	120.85
C(5)-C(6)-C(1)	120.71	120.94	120.44
C(5)-C(6)-C(7)	130.35	130.46	130.93
C(1)-C(6)-C(7)	108.89	108.60	108.63
C(2)-C(1)-C(6)	119.76	120.53	120.72
C(2)-C(1)-C(13)	129.92	129.13	129.70
C(6)-C(1)-C(13)	110.22	110.30	110.21
C(1)-C(2)-C(3)	119.07	118.36	118.53
C(4)-C(3)-C(2)	120.62	121.05	120.85
C(5)-C(4)-C(3)	121.00	120.90	120.68
C(4)-C(5)-C(6)	118.84	118.22	118.68

Table S4. Selected dihedral angles (°) obtained experimentally and calculated with PM3 and AM1 method for **4d**.

Dihedral Angle	X-ray	PM3	AM1
C(14)-N(1)-C(13)-C(12)	-62.83	-62.67	-47.39
C(17)-N(1)-C(13)-C(12)	169.74	167.48	148.75
C(14)-N(1)-C(13)-C(1)	54.62	54.90	47.39
C(17)-N(1)-C(13)-C(1)	-72.81	-74.94	-92.48
C(21)-C(20)-C(19)-C(18)	174.60	176.54	177.01
C(20)-C(19)-C(18)-O	-129.39	-106.44	-123.63
C(24)-C(19)-C(18)-O	44.53	-70.21	52.79
C(20)-C(19)-C(18)-N(2)	50.93	78.10	52.72
C(24)-C(19)-C(18)-N(2)	-135.16	-105.25	-130.85
O-C(18)-N(2)-C(15)	2.60	-22.25	-5.59
C(19)-C(18)-N(2)-C(15)	-177.74	-162.16	-178.07
O-C(18)-N(2)-C(16)	-171.44	-160.93	-160.37
C(19)-C(18)-N(2)-C(16)	8.20	23.48	23.28
C(18)-N(2)-C(15)-C(14)	128.0	-86.60	111.90
C(13)-N(1)-C(14)-C(15)	170.17	178.10	101.94
N(1)-C(13)-C(12)-C(11)	-53.80	-53.31	-57.41
N(1)-C(13)-C(12)-C(7)	126.42	128.66	125.89
C(18)-C(19)-C(24)-C(23)	-175.56	-178.00	-176.1,
C(18)-N(2)-C(16)-C(17)	-128.25	-108.00	-85.09
C(13)-N(1)-C(17)-C(16)	-170.31	-102.00	-177.48
N(1)-C(13)-C(1)-C(2)	61.30	55.00	54.40
N(1)-C(13)-C(1)-C(6)	-122.31	-126.00	-125.89

6. Antimycobacterial activity

MIC determination for the most potent *Mt*InhA inhibitors was accomplished *in vitro* using the *M. tuberculosis* H37Rv strain (**Table S5**). Although the poor solubility of the evaluated compounds precluded a more accurate MIC determination, piperazines **4b** and **4d** exhibited moderate antimycobacterial activity, with a MIC of 25 µg/mL (≈ 67.8 µM). These molecules have been previously reported with MIC values > 125 µM (**4b**) and 85 µM (**4d**) [1-2]. In addition, the MIC of lead-like compound **2** has been reported to be > 125 µM [1]; however, in our analysis, the maximum concentration achieved in solution was 12.5 µg/mL (35.2 µM). For compounds **4a**, **4f** and **4h-j**, the maximum concentration achieved in solution was 6 µg/mL, suggesting that the MIC values for these piperazines are greater than this value. A plausible hypothesis for the lower mycobacterial potency of these compounds is their deficient permeability through the mycobacterial cell wall and/or efflux pumps that extrude the compounds from the bacterial cell [1,3]. However, additional studies are necessary to clarify this aspect.

Table S5. MIC of the most potent synthesized piperazine-based *Mt*InhA inhibitors against the *M. tuberculosis* H37Rv strain.

Comp.	**MIC (µg/mL)/(µM)[a]**
2	> 12.5/> 35.2
4b	25/67.8
4d	25/67.8
4f	> 6/> 16.2
4h	> 6/> 16.1
4i	> 6/> 16.1
4j	> 6/> 15.3

[a]H37Rv is a drug-sensitive strain of *M. tuberculosis*.

6.1. Assessment of antibacterial activity

Select compounds were evaluated for the determination of the MIC against the *M. tuberculosis* strain H37Rv using a microtiter colorimetric assay. The select compounds were evaluated at different concentrations beginning with the maximum concentration allowed by the solubility of the compounds in a final DMSO concentration of 2.5% in each plate. The inoculum was prepared as previously described [4]. The resazurin microtiter assay (REMA) plate method was performed in 7H9 medium containing ADC (albumin, dextrose, and catalase). The plates were incubated at 37 °C, and after 7 days of incubation, a resazurin solution was added to each well, incubated for 48 h at 37 °C, and assessed for color development. Modification from blue color to pink indicates reduction of resazurin and, therefore, bacterial growth. The MIC value was defined as the lowest compound concentration that inhibits mycobacterial growth [4]. Growth

controls without antibiotic, sterility controls without inoculation, DMSO with inoculation, and an INH control were also included.

References:

[1] He, X.; Alian, A.; Ortiz de Montellano, P. R. Inhibition of the *Mycobacterium tuberculosis* enoyl acyl carrier protein reductase InhA by arylamides, **Bioorg. Med. Chem.**, v. 15, n. 21, 2007, p. 6649-6658.

[2] Muddassar, M.; Jang, J. W.; Hong, H. S.; Cho, Y. S.; Kim, E. E.; Keum, K. C.; Oh, T.; Cho, S.; Pae, A. N. Identification of novel antitubercular compounds through hybrid virtual screening approach, **Bioorg. Med. Chem.**, v. 18, n. 18, 2010, p. 6914-6921.

[3] Kuo, M. R.; Morbidoni, H. R.; Alland, D.; Sneddon, S. F.; Gourlie, B. B.; Staveski, M. M.; Leonard, M.; Gregory, J. S.; Janjigian, A. D.; Yee, C.; Musser, J. M.; Kreiswirth, B.; Iwamoto, H.; Perozzo, R.; Jacobs, W. R. Jr.; Sacchettini, J. C.; Fidock, D. A. Targeting tuberculosis and malaria through inhibition of enoyl reductase: compound activity and structural data, **J. Biol. Chem.**, v. 278, n. 23, 2003, p. 20851-20859.

[4] Palomino, J. C.; Martin, A.; Camacho, M.; Guerra, H.; Swings, J.; Portaels, F. Resazurin microtiter assay plate: Simple and inexpensive method for detection of drug resistance in *Mycobacterium tuberculosis*, **Antimicrob. Agents Chemother.**, v. 46, 2002, p. 2720-2722.